NSCL

NANOSCALE SYNTHESIS & CHARACTERIZATION LABORATORY

Annual Report 2007

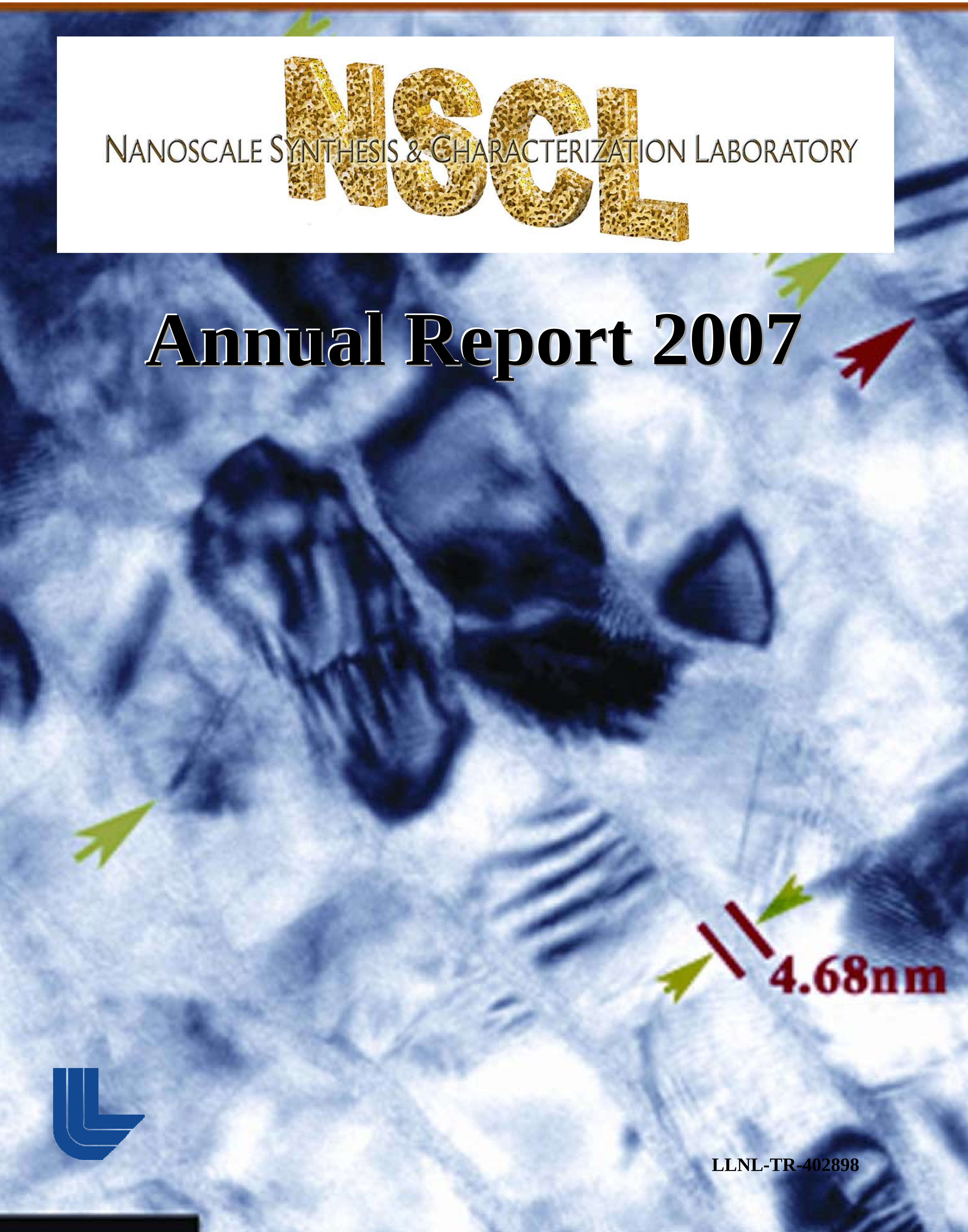

LLNL-TR-402898

Cover Photo:

Transmission electron microscope image of a copper/zirconium nanolaminate. The thickness of the CuZr glassy lay is shown.

Disclaimer

This document was prepared as an account of work sponsored by an agency of the United States government. Neither the United States government nor Lawrence Livermore National Security, LLC, nor any of their employees makes any warranty, expressed or implied, or assumes any legal liability or responsibility for the accuracy, completeness, or usefulness of any information, apparatus, product, or process disclosed, or represents that its use would not infringe privately owned rights. Reference herein to any specific commercial product, process, or service by trade name, trademark, manufacturer, or otherwise does not necessarily constitute or imply its endorsement, recommendation, or favoring by the United States government or Lawrence Livermore National Security, LLC. The views and opinions of authors expressed herein do not necessarily state or reflect those of the United States government or Lawrence Livermore National Security, LLC, and shall not be used for advertising or product endorsement purposes.

Auspices Statement

This work performed under the auspices of the U.S. Department of Energy by Lawrence Livermore National Laboratory under Contract DE-AC52-07NA27344.

By A. V. Hamza
Publication Date: April 2008

Nanoscale Synthesis and Characterization Laboratory Overview for FY2007

Alex Hamza
Director

Mission Statement: The Nanoscale Synthesis and Characterization Laboratory's (NSCL) primary mission is to create and advance interdisciplinary research and development opportunities in nanoscience and technology.

The NSCL is delivering on its mission providing Laboratory programs with scientific solutions through the use of nanoscale synthesis and characterization. While this annual report summarizes 2007 activities, we have focused on nanoporous materials, advanced high strength, nanostructured metals, novel 3-dimensional lithography and characterization at the nanoscale for the past 3 years. In these three years we have synthesized the first monolithic nanoporous metal foams with less than 10% relative density; we have produced ultrasmooth nanocrystalline diamond inertial confinement fusion capsules; we have synthesized 3-dimensional graded density structures from full density to 5% relative density using nanolithography; and we have established ultrasmall angle x-ray scattering as a non-destructive tool to determine the structure on the sub 300nm scale.

The NSCL also has a mission to recruit and to train personnel for Lab programs. The NSCL continues to attract talented scientists to the Laboratory. Andrew Detor from Massachusetts Institute of Technology, Sutapa Ghosal from the University of California, Irvine, Xiang Ying Wang from Shanghai Institute of Technology, and Arne Wittstock from University of Bremen joined the NSCL this year.

NSCL Staff: (left to right) Chris Walton, Luis Zepeda-Ruiz, Andrew Detor, Octavio Cervantes, Alex Hamza, Robin Miles, Matt Bono, Sutapa Ghosal, Juergen Biener, Andrea Hodge, Arne Wittstock, Yong Han, Morris Wang, Alex Chernov, Sergei Kucheyev, and Greg Nyce. Missing: Ted Baumann, Monika

Biener, Tony van Buuren, George Gilmer, Joe Satcher, Don Lesuer, Troy Barbee, Babak Sadigh, Marcus Worsley and Xiang Ying Wang.

The NSCL is pursuing four science and technology themes: nanoporous materials, advanced nanocrystalline materials, novel three-dimensional nanofabrication technologies, and non-destructive characterization at the mesoscale. The NSCL is also pursuing building new facilities for science and technology such as nanorobotics and atomic layer deposition.

We continue to lead in the synthesis and characterization of nanoporous metals. We have discovered, developed, and refined an array of synthesis approaches for nanoporous metals with relative densities below 25% and pore sizes on the nanometer length scale. Nanomechanical characterization techniques and catalytic characterization have led to the exciting discovery of novel chemical actuation of nanoporous metals.

Another area of expertise is the development of advanced nanocrystalline materials synthesis. We have used electrodeposition and sputtering techniques to successfully synthesize nanocrystalline Au/Cu alloy and Cu/Zr nanolaminates. Both of these materials exhibit excellent hardness and tensile strength properties. The deformation mechanisms of these materials with grain sizes of 10-20 nm and below are being addressed through molecular dynamics models.

Development of novel 3-D nanoscale fabrication techniques is the third main theme of the NSCL. We have established new tools for 3-D fabrication such as focused ion beam processing and proximity field nanopatterning.

Nondestructive, mesoscale characterization is the fourth main theme of the NSCL. We are establishing new tools in x-ray imaging and scattering techniques to provide nanoscale to microscale characterization.

Highlights for FY07

In FY07 we have had another productive year, making progress in our four theme areas: nanoporous materials, advanced nanocrystalline materials, novel 3D fabrication and mesoscale characterization. Below are a few highlights.

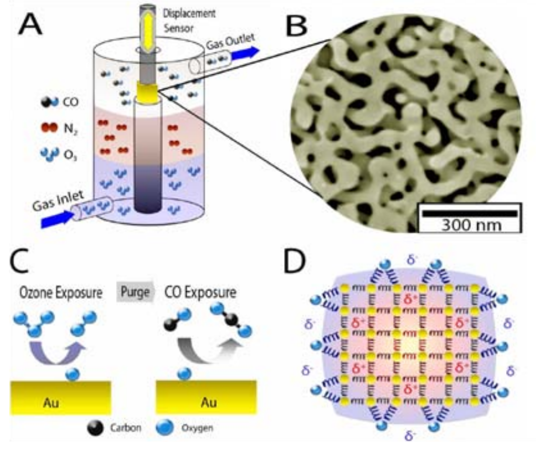

*Figure 1 Illustration of surface chemistry driven actuation in nanoporous gold. (**A**) Np-Au sample mounted in a viscous flow reactor (residence time ~ 1min). Adsorbate-induced dimensional changes of the np-Au sample are measured by dilatometry. (**B**) SEM micrograph showing the characteristic sponge-like open-cell morphology of np-Au. (**C**) Au surfaces can be switched back and forth between an oxygen-covered and clean state by alternating exposure to ozone (O_3) and carbon monoxide (CO). (**D**) Spring model illustrating the origin of adsorbate induced surface stress. Adsorbate-induced changes in the equilibrium distance a_o between surface atoms give rise to tensile ($a<a_o$) or compressive ($a>a_o$) surface stress.*

We have demonstrated that surface chemistry driven actuation can be realized in high surface area materials such as nanoporous gold. We achieved reversible strain amplitudes in the order of a few tenths of a percent by alternating exposure of nanoporous Au to ozone and carbon monoxide. The effect can be explained by adsorbate-induced changes of the surface stress, and can be used to convert chemical energy directly into a mechanical response thus opening the door to surface-chemistry driven actuator and sensor technologies.

This year has seen continued progress in the technology and science for crystalline carbon (diamond) ablator capsules. In collaboration with the Fraunhofer Institute for Applied Solid State Physics we have developed techniques to polish nanocrystalline carbon shells to very low roughness (<10 nm rms). Figure 2 shows a fourier transform of a series of height traces around these nanocrytalline carbon ablators, comparing to NIF standards for Be, high density carbon (HDC), and plastic (CH) capsules to the measured roughness of high density nanocrystalline carbon capsules.

We have developed a novel technique to join on the micron to nanometer scale. Joining foam is a challenge because bonding agents are often wicked many microns into the foam. We used vapor deposition of a solder on both the copper foam component and the aluminum component. With precision fixtures to apply sufficient pressure and temperature, the components were bonded. A cross-section was focused ion beam machined into the material to expose the interface, as shown in Fig. 3. The solder is evident between the foam and the substrate, and the two layers of solder that had been deposited on the individual components have melted together to form a single layer with a thickness of approximately 1.5 μm. The solder did not wick into the foam to any significant extent, and there are no voids in the foam at the interface larger than a few μm.

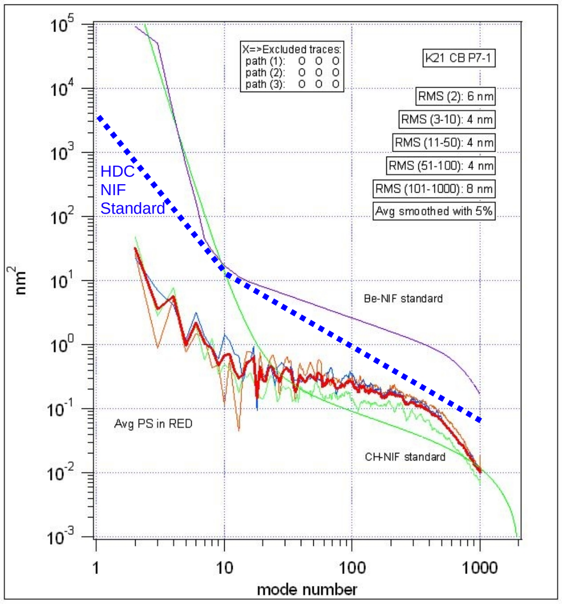

Figure 2: Fourier transform power spectrum for height traces around nanocrystalline carbon shells. RMS roughness is below 10 nm for all modes.

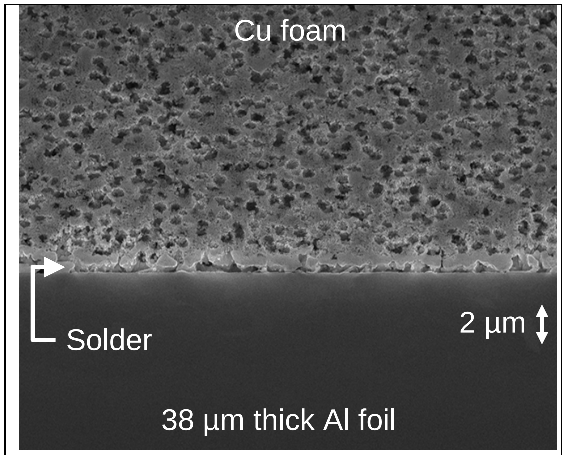

Figure 3: SEM image of the bonded interface between the copper foam and the aluminum foil

Plans for FY08

For the coming fiscal year the major focus in the NSCL will be to deliver on the strategic initiative, "Nanomaterials for Fusion Application." The strategic initiative focuses on "chemistry-in-a capsule," tailored doping, robotic nanomanipulation, forming cryogenic layers in foam, and low stress thick film growth.

We will establish atomic layer deposition and nanorobotic capabilities at LLNL in FY08. We will also continue our pursuit of understanding of the behavior of quantum solids (hydrogen) and their interaction with substrates.

The NSCL is primarily funded by LDRD investments and Tech Base/Materials Technology Projects.

Nanoscale Synthesis & Characterization Laboratory Annual Report 2007

Table of Contents

Incipient plasticity in Cu/Zr nanolaminates

Y.M. Wang, A.V. Hamza, T.W. Barbee, Jr.

The plastic deformation in Cu-Zr nanocrystalline - amorphous nanolaminates is investigated by means of stress-relaxation experiments at a range of initial stress levels. Progressive multi-step relaxation cycles reveal that the onset of plastic deformation occurs at a much lower stress level in nanocrystalline-amorphous nanolaminate than in crystalline-crystalline nanolaminates or other nanostructured materials. This indicates that the crystalline-amorphous interfaces may be the preferred source for dislocation nucleation and/or emission.

The nanocrystalline-amorphous Cu/Zr nanolaminate samples were fabricated using magnetron sputtering. Solid state amorphization process allows controlled fabrication of nanolaminates with different amorphous and nanocrystalline individual layer thickness. The stress-relaxation experiments at stress intervals of 100 MPa were carried out in an Instron 4444 desk-top tensile apparatus at room temperature. Figure 1 shows the progressive stress-relaxation cycles of the 5/35 Cu/Zr nanolaminate (i.e., 5 nm amorphous layer and 35 nm nanocrystalline Cu layer) at the stress interval of 100 MPa. At low stress levels (<220 MPa), the deformation of the sample is in the elastic regime and therefore no detectable stress decay is observed. Starting at the stress level of ~320 MPa, however, the stress decay as a function of time becomes increasingly distinguishable, with the higher stress decay rate occurring at higher stress levels. We believe that such stress-relaxation behavior has not been observed before in conventional stress-relaxation experiments and is a direct consequence of the unique behavior of these amorphous-crystalline interfaces in determining the observed mechanical properties. The lower stress required for incipient plasticity in nanocrystalline - amorphous nanolaminates is a strong indication that the crystalline-amorphous interface has the unique properties in generating or absorbing dislocations that is otherwise impossible in crystalline-crystalline interfaces or grain boundaries or twin boundaries. This work provides insights on the interesting properties of amorphous-crystalline interfaces in determining the dislocation behavior and thus controlling the plastic deformation of amorphous-crystalline nanolaminates. We expect that our results have implications to help design strong and ductile amorphous-crystalline nanocomposites.

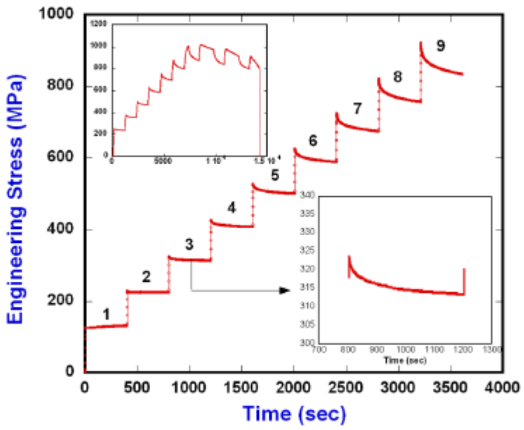

Figure 1 Progressive stress-relaxation plots of Cu/Zr crystalline-amorphous nanolaminates, showing the early incipient plasticity.

Reference:

1. Y.M. Wang, A.V. Hamza, T.W. Barbee Jr., *Appl. Phys. Lett.*, 061924 (2007).
2. Y.M. Wang, J. Li, A.V. Hamza, T.W. Barbee Jr., *PNAS* 104 (27), 11155-11160 (2007).

Effect of surface instability on stress in sputtered thick films

George Gilmer, Luis A. Zepeda-Ruiz, Andrea Hodge, Chris Walton, Morris Wang, Andy Detor, Hongwei Xu (General Atomic), Abbas Nikroo (General Atomic) and Eric Chason (Brown University)

"Thick" films (on the order of 100's of microns) are critical for many emerging applications, such as targets for the national ignition facility (NIF). Thick films can be deposited by conventional thin film deposition techniques such as sputtering, but the longer deposition times and thicker structure present unique challenges. In particular, controlling the stress is critical to prevent cracking or delamination and controlling the surface morphology is necessary to obtain the required smoothness.

We have used a combination of computer simulations and experiments to study the processes controlling stress and surface morphology during the deposition of sputtered films. We find that barriers to surface diffusion between different layers (known as Ehrlich-Schwoebel or ES barriers) can make the surface morphology susceptible to an instability which transforms the growth from smooth layers to pillar-like columns. The gaps between these columns prevent complete densification which can lead to the trapping of porosity in the layer. This has the effect of preventing atoms from being able to transport into the grain boundaries between the layers and results in tensile stress in the film. Experiments on sputtered Be films confirm the presences of a transition from smooth growth to a columnar structure as the film gets thicker. Concurrent measurements of the stress show how the morphological change couples to the stress evolution. Such studies suggest that modifications to the growth to prevent the onset of the roughening instability will enable the buildup of stress to be slowed and also decrease the porosity trapped in the film.

Kinetic Monte Carlo (KMC) computer models were used to simulate the thin film growth under different conditions (figure 1). The different colors correspond to differently oriented polycrystalline grains in the simulated material. In the absence of ES barriers to interlayer diffusion, the simulated surface is observed to remain smooth during growth (figure 1a). When an ES barrier of 0.1 eV is present, the surface morphology changes significantly (figure 1b). Although both surfaces look similar in the early stages, the ES barrier makes the surface break up into mounds which become columns in the resulting microstructure. Without ES barriers, the grain size generally increases with film

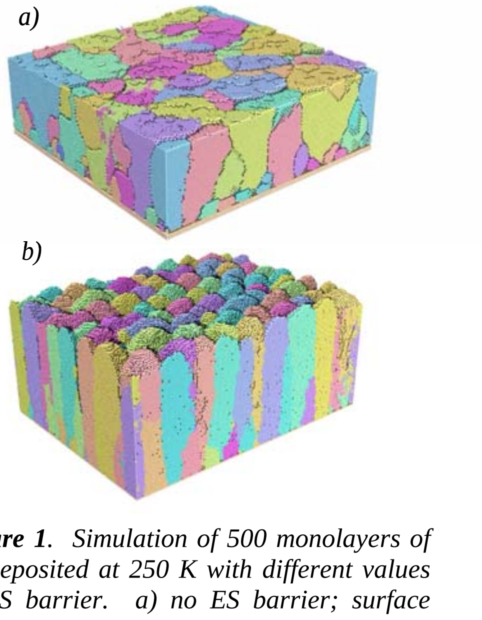

***Figure 1**. Simulation of 500 monolayers of Be deposited at 250 K with different values of ES barrier. a) no ES barrier; surface remains smooth indefinitely. b) ES barrier = 0.1 eV; surface roughens after appr. 100 layers.*

thickness while the presence of ES barriers produces columns that increase in width more slowly with the film's thickness. Equally important, the columnar structure makes it difficult for newly-deposited atoms to diffuse into the region between them and create a fully dense structure. The simulations show that this causes vacancies and voids to get trapped in the film. This imperfect densification can contribute to the generation of tensile stress in the film.

Experiments on Be films display the behavior predicted by the simulations. Be films were sputtered onto Si(100) substrates and measurements of the stress were obtained during the growth using an *in situ* wafer curvature technique. This method monitors the bending of the substrate during growth which is related to the product of the film stress and film thickness. The results (figure 2a) show a very significant change in the stress state of the film as the thickness increases. For the thinner film, the stress is largely compressive with a maximum value of 1.6 GPa. However, as the thickness increases and the columns become more separated, the stress is strongly modified and becomes highly tensile in the upper layers (as large as 0.56 GPa). The corresponding surface microstructure is shown in the accompanying SEM images (figure 2b). The thinner film is clearly smoother while the thicker film shows the onset of a mounding instability similar to the one seen in the simulations. Cross-sections of the thicker films confirm that the microstructure is primarily columnar.

The strong coupling between the morphology and the stress generation in the film explains how the stress can change from compressive to tensile even though the deposition conditions have not been changed. Moreover, these results provide a way to understand what controls the onset of the roughening instability. Suppressing the roughening can provide a practical method for controlling the film stress and enable the growth of thick films with the mechanical strength and resistance to gas permeation needed for NIF targets and other applications.

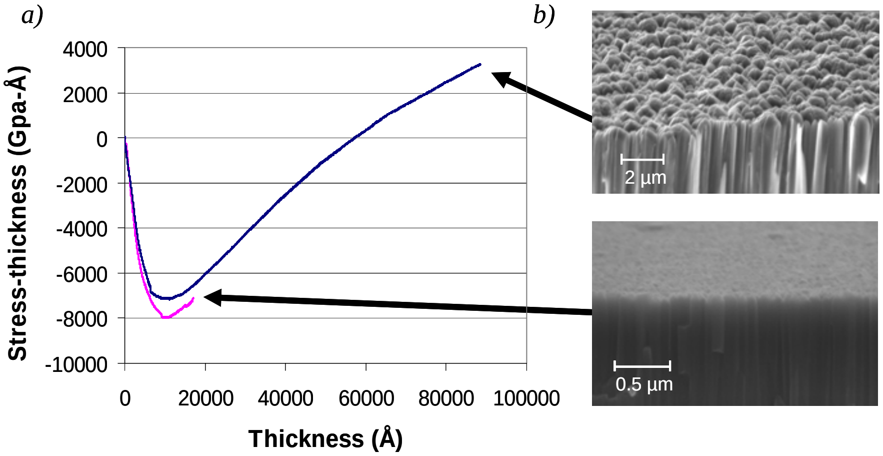

Figure 2. *a) Evolution of stress-thickness (product of film stress and film thickness) for thin and thick Be films grown under the same conditions. The stress state changes from compressive to tensile as the thickness increases. b) SEM of surface structure after growth terminated at thickness indicated by arrows.*

Surface morphology evolution during sputter deposition of thin films

Luis A. Zepeda-Ruiz and George H. Gilmer

The vapor growth of uniform thin films on foreign substrates is impeded by several morphological instabilities. Hill-and-valley structures are often formed as a result of (1) the Grinfeld instability, where the film is under stress due to lattice mismatch, (2) the shadowing instability, which inhibits the full coalescence of three dimensional islands formed during initial growth, and (3) the Ehrlich-Schwoebel (ES) instability, which results from a larger barrier to adatom diffusion across a step edge than that for diffusion on the terraces between steps. These instabilities are enhanced during the growth of thick films, such as the Be shells for NIF targets, where surface height perturbations have an opportunity to grow to large amplitudes.

We have developed a kinetic Monte Carlo (KMC) model based on the HCP lattice of Be, that allows us to simulate the growth of Be films, and include the physical mechanisms leading to the morphological instabilities. Our KMC simulations show that while surface roughness can be controlled by changing growth conditions, such as growth temperature and the angular distribution of the impinging particles, the ability of the particles to diffuse over step edges, plays a very important role in controlling the density of the films.

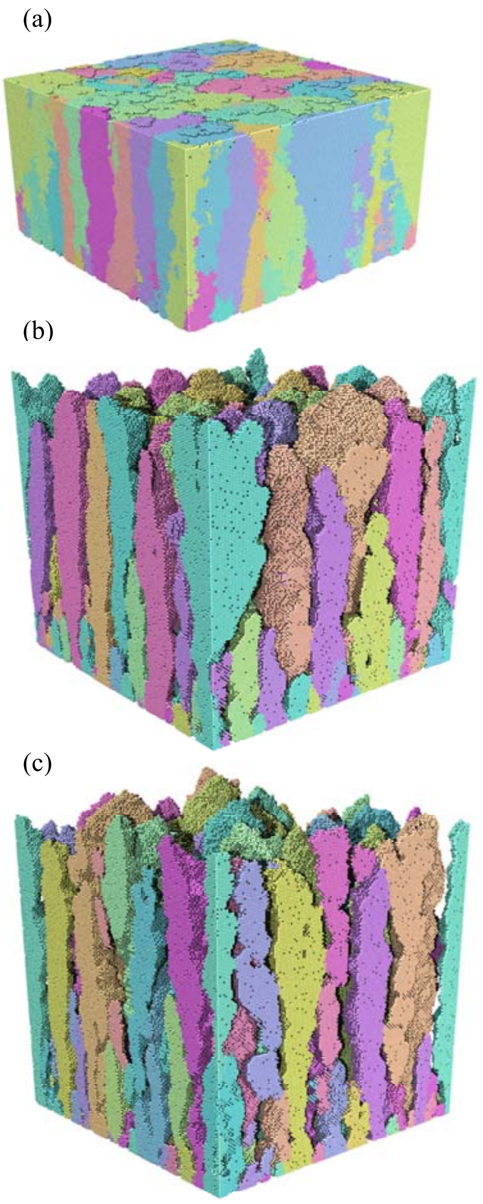

Figure 1. Snapshots of the Be film after deposition of 2.25x10^6 Be atoms at 175 K with different values of ES barrier. a) ES barrier = 0, b) ES barrier = 0.1 eV and c) ES barrier = 0.2 eV.

Figure 1 shows three different films obtained after deposition of 2.25x10^6 Be particles at a temperature of 175 K for different values of the ES barrier. In all three cases, growth starts by nucleation of islands with different orientations (denoted by different colors) that coalesce as growth proceeds. In the absence of an ES barrier, the surface of the resulting film is smooth (Fig. 1a). As the ES barrier increases, a growth instability appears and growth changes from smooth layers to columnar grains (Figs. 1b and 1c). At this low temperature diffusion along grains is very difficult resulting in grains of different heights. Since the angular distribution of the incoming particles is according to a cosine distribution, the difference in height of the grains produces a shadowing effect that makes incorporation of material into the gaps between the grains extremely difficult. This results in a highly porous film.

Figure 2 shows the Be films grown at a temperature of 250 K for the same three magnitudes of the ES barrier of Fig. 1. At this temperature surface diffusion is enhanced. This results in a different growth mode characterized by the presence of very dense mounds (for Es > 0). As growth proceeds, due to the shadowing effect some of these mounds are pinched off and deep grooves are observed.

In conclusion, we showed that the surface morphology and porosity of thin Be films strongly depends on growth conditions and material properties. Our KMC simulations provide a way to understand the factors that give rise to the onset of surface instabilities during sputter deposition of thin films.

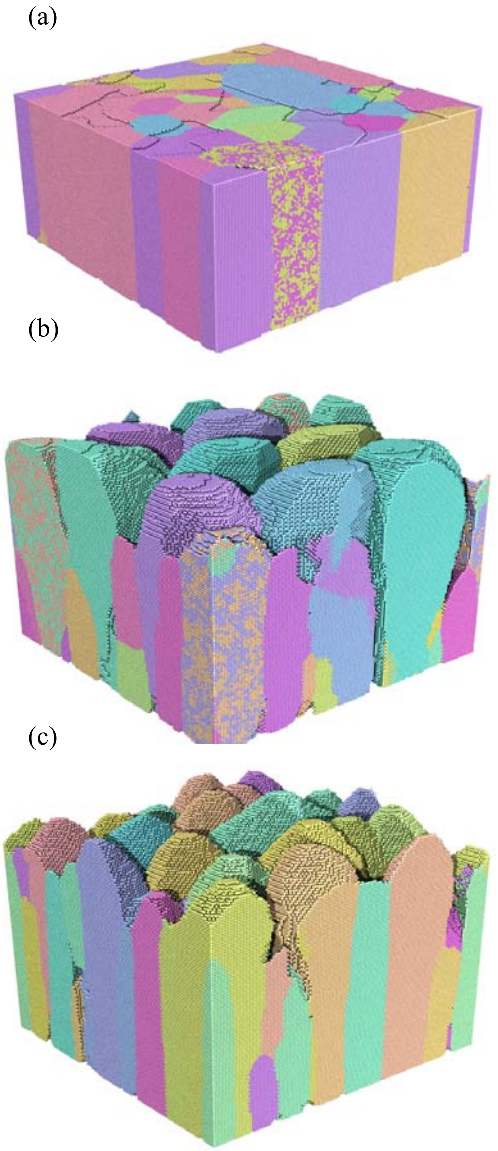

Figure 2. Snapshots of the Be film after deposition of 2.25x10^{6} Be atoms at 250 K with different values of ES barrier a) ES barrier = 0, b) ES barrier = 0.1 eV and c) ES barrier = 0.2 eV.

Thick, Uniform Gold-Copper-Tin Alloy Coatings on Hollow Glass Mandrels for Double-Shell Target Development

P. Mirkarimi, K. Bettencourt, J. Hayes, Y.M. Wang, and A.V. Hamza (LLNL), Martin Hoppe and Abbas Nikroo (GA)

$Au_xCu_ySn_z$ coated hollow glass mandrels can serve as the inner shell of a double shell target design for ICF/NIF. The films need to be of uniform thickness and at least several tens of microns thick, of the correct composition, and sufficiently smooth. In order to hold the high-pressure DT gas, high strength is also required for these films. $Au_{0.62}Cu_{0.34}Sn_{0.04}$ alloy films were deposited on ~1 mm diameter hollow glass spheres by sputter deposition, as shown in Figure 1a.

(a)

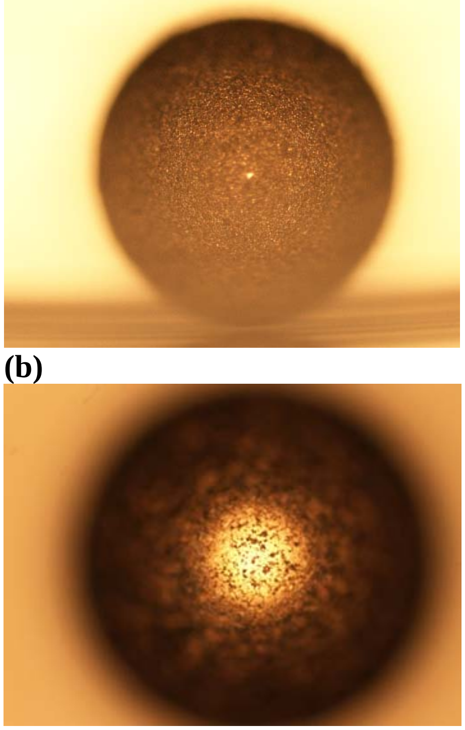

Figure 1 Optical micrographs of (a) as-deposited and (b) polished $Au_xCu_ySn_z$ coated hollow glass spheres.

This alloy composition is expected to maintain good strength due to intermetallic formation from the Au-Cu, and inhibition of grain growth during annealing/filling by the addition of a small amount of Sn. Initial attempts at polishing were promising; the coated sphere shown in Figure 1b had smooth finish.

Metallurgical cross-sectioning demonstrated that the coatings were uniform and ~35 microns thick. The thickness was confirmed by FIB measurements, as shown in Figure 2.

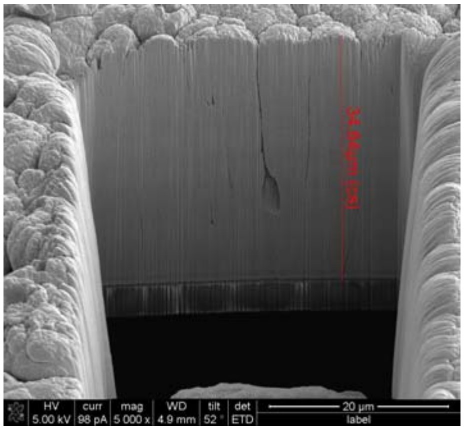

Figure 2 Focused ion beam analysis on a gold sphere demonstrating that a thickness of ~35 microns was achieved.

$Au_{0.62}Cu_{0.34}Sn_{0.04}$ films were also deposited on flat glass substrates under the same deposition conditions: one set was left untouched and one set annealed at ~ 300 C for ~ 48 hrs, similar to annealing conditions for the fill. Mechanical property measurements indicate that the hardness of the alloy increases from 2.5 GPa to 3.2 GPa. The enhanced hardness after annealing is rather interesting and shows the promise of this material for our applications.

In-situ residual stress measurements in beryllium films

Y.M. Wang, A. Detor, A.M. Hodge, E. Chason (Brown Univ.), C. Walton, A.V. Hamza, H.W. Xu (GA), A. Nikroo (GA)

To understand the residual stress and microstructure evolution in beryllium films is of fundamental importance for developing high-quality, leak-proof beryllium capsules for high-energy target applications. The typical problems that are associated with the beryllium film quality include high residual stresses, rough surface, argon-gas trapping. To investigate these issues, we have applied an in-situ residual stress measurement technique (MOS system at General Atomics) to monitor the stress evolution as a function of as-grown film thickness under different sputtering conditions. We have investigated the effect of Argon sputtering pressure, biasing condition, substrate temperature, sputtering power, number of guns, and the type of substrates on the evolution of the residual stresses and microstructures in Be films.

In general, we found the following effect for each deposition parameters: (a) *sputtering pressure*: within the pressure range we investigated (2-10 mTorr), lower pressures result in more compressive stress. This observation is consistent with most other documented findings in the literature; (b) *substrate temperature:* in this set of experiments, we varied the substrate temperature from room temperature to 300 ^{o}C and found that higher substrate temperature results in more compressive stresses. In addition, we noticed the dramatic change in surface structure: as temperature increases, the surface becomes much more faceted; (c) *bias:* biasing leads to compressive stress. This can be shown representatively in Figure 1. The surface structure also appears (similar to the temperature effect) to be more faceted with biasing, suggesting enhanced mobility of the surface atoms. (d) *sputtering power:* within the range of power we studied (100-200 W), we did not observe a clear trend. The change of microstructures is not very obvious with an increase/decrease in power. The limited 100 W range covered is apparently insignificant; (e) *number of guns:* when other sputtering conditions are the same, more guns (3 guns) lead to more compressive stresses. This is consistent with “atomic peening” models of compressive stress which scale with the deposition flux. There is also a substantial change in the surface structure where the 3 gun specimen has much sharper and well defined (faceted) features as compared to the 1 gun case; (f) *type of substrates:* up to date, we have investigated three types of different substrates: silicon (100), silicon (111), and MgO (100). One common trend we have seen so far is the reduction of the thermal stress component by using MgO substrate, as it has similar thermal expansion coefficient to that of beryllium film.

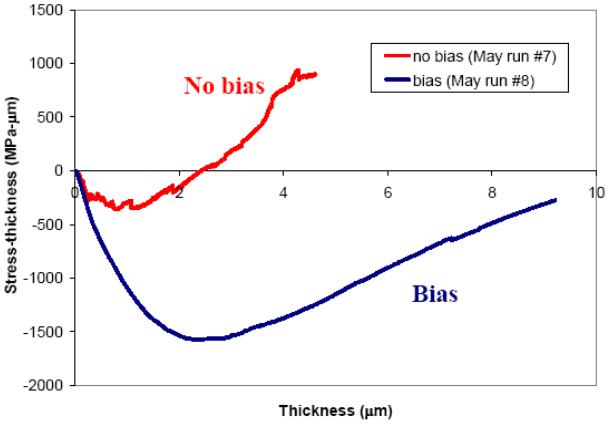

Figure 1 Effect of bias on the residual stress of Be film at room temperature.

Synthesis of thick, low-stress tantalum films

Andrew Detor, Andrea Hodge, Morris Wang, Ron Foreman, Allen Elsholz, Alex Hamza

Tantalum has found widespread use in the electronics industry as a thin film diffusion barrier, exploiting its refractory metal properties in preventing contamination of semiconductor junctions [1]. While this technology is relatively mature, other applications requiring thicker films have had less success due to high residual stresses that build up with thickness, causing cracking or spalling in the extreme cases of tension or compression, respectively. The root cause of these stresses at the microstructural level remains poorly understood, preventing the synthesis of high quality films as required, for example, in wear-resistant coating applications and for fundamental studies of material behavior. In the present work we combine *in-situ* and *ex-situ* stress measurements with detailed microstructural characterization in order to elucidate the stress-generating mechanisms, with the ultimate goal of achieving thick (~100 μm), low stress tantalum deposits.

Specimens are produced using a magnetron sputtering technique where stress can be quantified based on substrate curvature. Results from *ex-situ* profilometry measurements are shown in Fig. 1 plotting stress as a function of sputtering gas pressure and target power. The trends here are consistent with those found in the literature for a variety of systems [2, 3] where a decrease in pressure and/or increase in power leads to more compressive stress. It is important to note that both tensile and compressive states have been accessed in these experiments, suggesting that a zero stress condition may be achieved through judicious control of the process variables.

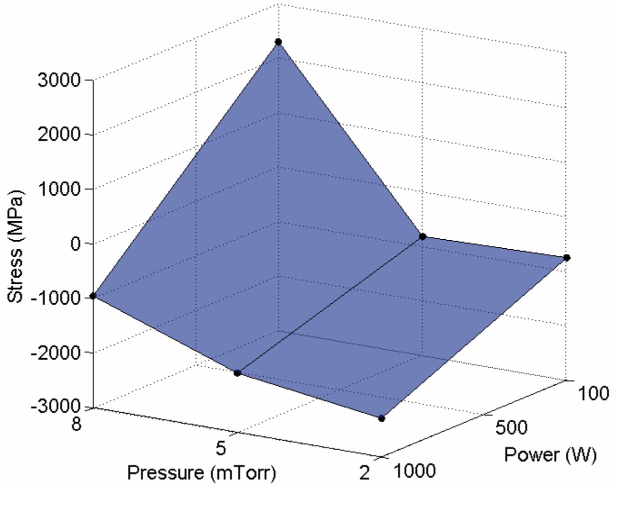

Figure 1: Average stress in magnetron sputtered tantalum films as a function of gas pressure and target power. A state of zero stress should be possible through optimization of both variables.

Although the *ex-situ* measurements of Fig. 1 are useful in terms of understanding the stress state following deposition, we are also interested in how this stress evolves with thickness. For this we employ a laser reflection technique [4] to characterize the substrate curvature *in-situ*, during the sputtering process. Typical results are shown in Fig. 2 for experiments conducted at 100 W power and pressures of 2 and 5 mTorr, both of which yield similar *ex-situ* stress levels (see Fig. 1). Here it is obvious that the stress evolution is more

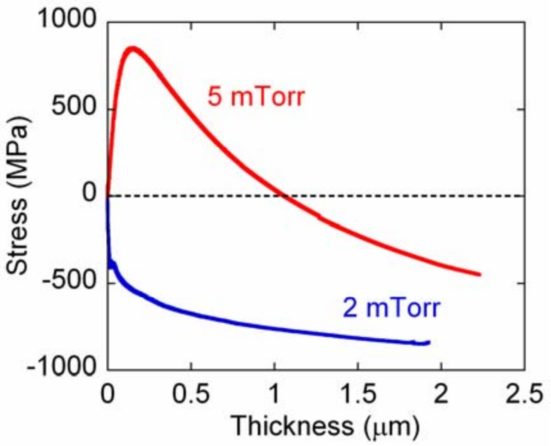

Figure 2: Stress measured *in-situ* for specimens sputtered under 2 and 5 mTorr pressure at 100 W. Tension-compression transitions such as that shown for the 5 mTorr specimen would not be observed through traditional *ex-situ* techniques.

complex than the *ex-situ* measurements suggest. While the low pressure specimen is exclusively compressive, the high pressure specimen exhibits a tensile-to-compressive transition. Understanding the microstructural features responsible for this kind of behavior is one of the main goals of the present work.

To characterize the microstructure we employ a variety of techniques including x-ray diffraction, transmission (TEM) and scanning (SEM) electron microscopy, and focused ion beam (FIB) microscopy. Preliminary results of a SEM-FIB investigation are shown in Fig. 3. The top figure (a) shows the surface structure of a tantalum specimen revealing nanometer scale features. In (b) a FIB cross-section is used to measure film thickness and also observe any possible flaws such as cracking or porosity.

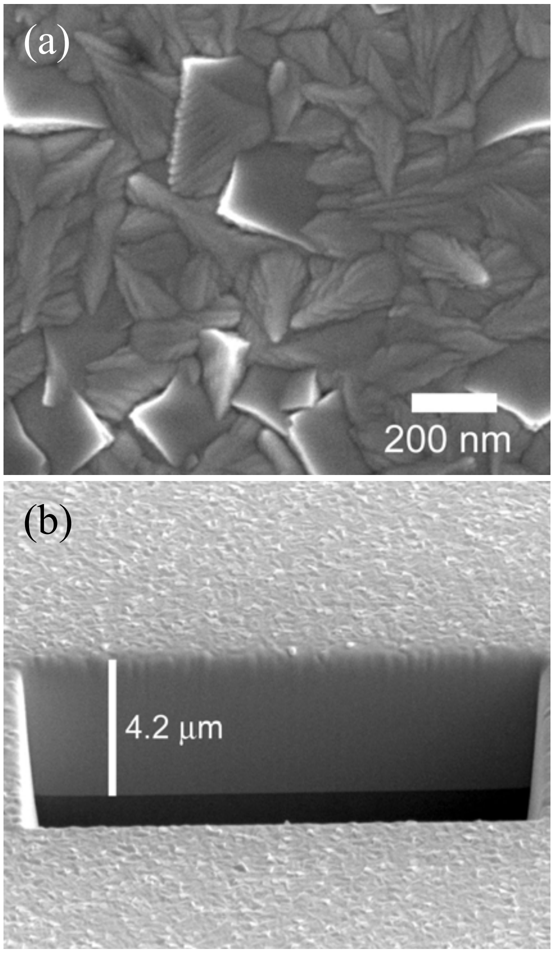

Figure 3: (a) Surface structure of sputtered tantalum as observed by high resolution SEM. (b) A FIB milled trench used to investigate film thickness and quality. These and future microstructural investigations will be used to understand the stress generating mechanisms in thick films.

Future investigations will extend the micro-machining capabilities of the FIB as an additional means to characterize residual stresses, as well as exploit the unique advantages of ion beam imaging to observe grain structure. Correlating these microstructural investigations with *in-situ* and *ex-situ* stress measurements, as well as computational and theoretical efforts, will add to our understanding of the fundamental mechanisms responsible for stress generation in thick film deposition.

References

1. Holloway, K. and Fryer, P., *Tantalum as a Diffusion Barrier between Copper and Silicon.* Applied Physics Letters, 1990, **57**(17), p. 1736-1738.
2. Hoffman, D.W., *Perspective on Stresses in Magnetron-Sputtered Thin-Films.* Journal of Vacuum Science & Technology A, 1994, **12**(4), p. 953-961.
3. Windischmann, H., *Intrinsic Stress in Sputter-Deposited Thin-Films.* Critical Reviews in Solid State and Materials Sciences, 1992, **17**(6), p. 547-596.
4. kSA Multi-beam optical sensor (MOS) system, k-Space Associates, Inc., www.k-space.com.

Atomistic simulations of grain coalescence: a mechanism for tensile stress generation in deposited films

Andrew Detor

Materials produced by deposition techniques are often plagued by high levels of tensile stress. Beginning with the early work of Hoffman [1], a number of researchers have analytically modeled the physical origin of this stress as a direct consequence of grain boundary coalescence, assuming that some attraction between the free surfaces of neighboring grains during film formation causes a spontaneous gap closure, leading to a net in-plane contraction of the film. A simple thermodynamic analysis by Nix and Clemens [2] gives the stress, σ, as:

$$\sigma \approx \left[\frac{4E(2\gamma_s - \gamma_{gb})}{d}\right]^{\frac{1}{2}} \tag{1}$$

where E is Young's modulus, γ_s and γ_{gb} are the surface and grain boundary energies, respectively, and d is the grain size of the film. The fundamental driving force for this mechanism is a reduction in the system energy when grain boundaries replace free surfaces, with the requirement that $\gamma_{gb} < 2\gamma_s$ in Eq. (1). Although these kinds of models have been used to explain the stresses observed in experiments, the atomic level mechanisms involved are difficult to access and not well understood. In the present work we explore these mechanisms by way of atomistic computer simulations.

A schematic of the simulation setup is shown in Fig. 1. Two grains, A and B, are constrained between fixed plates with periodic boundary conditions in the x-z plane of the grain boundary. After an initial rigid displacement (offset), the grains A and B are allowed to relax by a molecular statics conjugate gradient routine. Atomic interactions are governed by a multi-body potential for tantalum, so as to provide realistic behavior and energy levels for this material. Following full relaxation of the structure, details of the atomic positions, energy, strain, and stress produced due to coalescence can be analyzed as a function of the initial offset. In total, 11 unique <110> symmetric tilt boundaries will be simulated in this work, spanning a range of misorientations from ~6-75 degrees.

Initial results for a low-angle boundary are shown in Fig. 2 where normal strain in the y-direction is plotted on a color scale. As expected, the structure with a comparatively large offset of (b) 0.17 nm displays higher strain levels than that in (a), where no offset has been applied. It is also clear that the grain boundary in (b) contains more free volume than that in (a), suggesting important potential differences in the mechanical and transport properties of these boundaries.

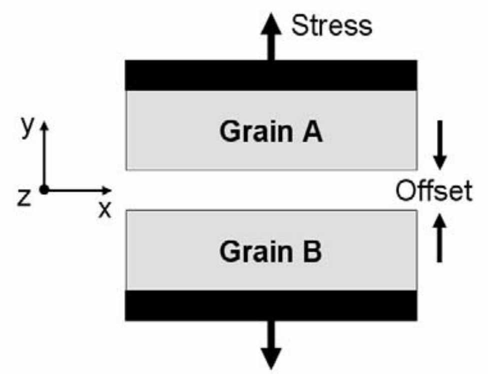

Figure 1: Schematic of the simulation setup. Grains A and B are held between fixed plates and allowed to relax after an initial rigid displacement.

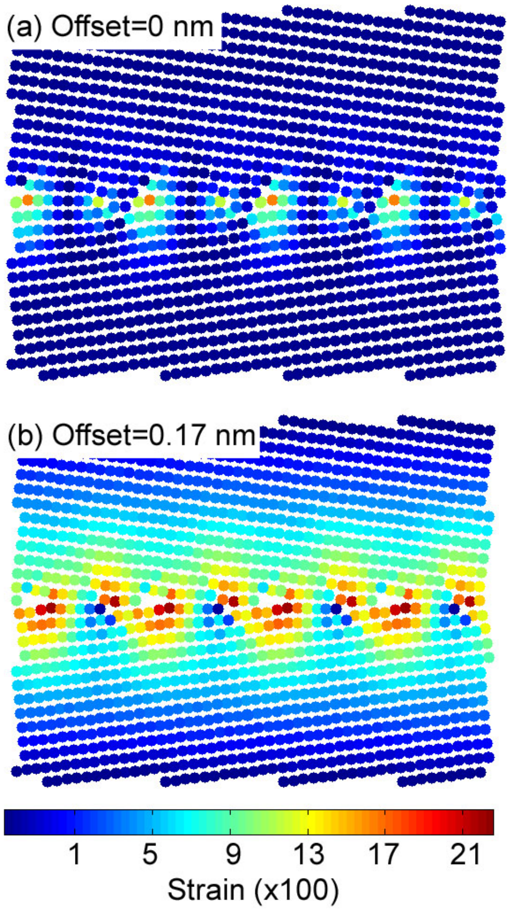

Figure 2: Atomic-level strain produced upon relaxation of a Ta <110>, Σ73(661) tilt boundary after initial offsets of (a) 0 and (b) 0.17 nm. Higher strain and stress (see Fig. 3) levels occur with increasing offset.

Following coalescence, the average stress developed on the fixed plates can be measured, as indicated in Fig. 1. Results for the present low-angle boundary are shown in Fig. 3 where stress is plotted as a function of the initial offset amount. Stress is observed to increase linearly with offset, reaching a maximum value of ~2 GPa, reasonably in line with the levels observed in experiments under conditions promoting high tensile stress. Beyond the maximum offset shown in Fig. 3 no coalescence is observed as the atomic interactions are insufficient to "close the gap" at this range (>0.17 nm).

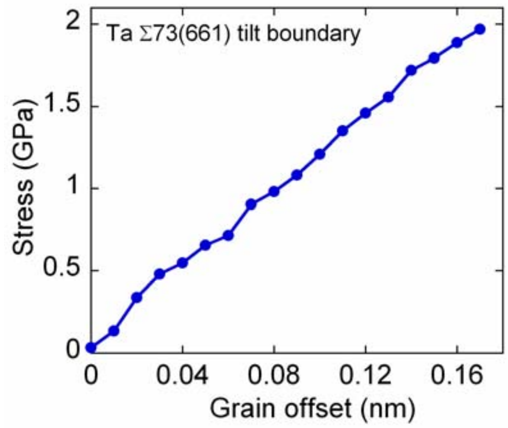

Figure 3: Stress measured after grain coalescence for the Ta boundary shown in Fig. 2 as a function of the initial offset. High stresses approaching 2 GPa are produced, in line with those measured in experiments

Comparing results such as those shown in Figs. 2 and 3 across a range of unique grain boundaries will provide important information that can be correlated with existing analytical models. For example, Eq. (1) suggests a strong dependence on the difference between surface and grain boundary energy, quantities that can be directly measured in these simulations. Also, the structures obtained at various offsets may be subject to external mechanical loads to study how deformation mechanisms change for non-equilibrium boundaries. Investigations such as these will help shed light on the physical behavior and stresses observed in experimentally deposited specimens.

References

1. Hoffman, R.W., *Stresses in Thin-Films - Relevance of Grain-Boundaries and Impurities.* Thin Solid Films, 1976, **34**(2), p. 185-190.
2. Nix, W.D. and B.M. Clemens, *Crystallite coalescence: A mechanism for intrinsic tensile stresses in thin films.* Journal of Materials Research, 1999, **14**(8), p. 3467-3473.

Abnormal strain hardening in nanostructured titanium at high strain rates and large strains

Y. M. Wang, J. Y. Huang (Boston College), T. Jiao (Brown Univ.), Y. T. Zhu (LANL), A. V. Hamza

Commercial purity nanostructured titanium prepared by equal channel angular pressing plus cold rolling (grain size ~260 nm) exhibits a nonnegligible strain hardening behavior at large compressive strains (>15%) and quasistatic loading conditions. The degree of the strain hardening increases with increasing strain rates and becomes more pronounced at dynamic loading rates. This behavior is in contrast with what we have seen so far in other nanostructured materials, where flat stress-strain curves are often seen. It was concluded from transmission electron microscopy investigations that in addition to dislocation slips, deformation twinning may have played a significant role in plastic deformation of nanostructured Ti. The structural failure behavior is in-situ recorded by a CCD camera and reasoned according to the microscopic observations.

In this study, we investigated the mechanical properties of nanostructured Ti to much larger strains and a wide range of strain rates in order to understand what factors and how they control the deformation/failure behavior of UFG-Ti. We paid special attention on the possibility of twinning activities in nanostructured Ti that were overlooked in the literature. In order to do so, an in-situ high speed camera was employed in the experiments so as to capture the evolution of surface micrographs in UFG-Ti during dynamic compressions. The postmortem microstructures at different strains were examined by transmission electron microscopy (TEM). The results were used to interpret the deformation mechanism and failure mode of UFG-Ti.

Figure 1 shows true stress-strain curves of UFG-Ti with the strain rate in the range of 10^{-4} s^{-1}–10^{-1} s^{-1}. For comparison, the stress-strain curve of a coarse-grained (CG) Ti is also included. A considerably elevated strength was observed in UFG-Ti with the yield stress 3–4 times higher than that of CG-Ti. In terms of ductility, UFG-Ti fails after a total compressive strain of ~30%, as compared to ~60% in CG-Ti and ~10% in nanostructured Fe. Such ductility is consistent with what we have seen so far in other nanostructured metals, where a notable reduction of tensile/compressive strain to failure was observed as a result of nanostructuring. Significantly, we also observed an unusual strain hardening behavior in nanostructured Ti after 15% strains and at all strain rates. TEM investigation suggests that such strain hardening behavior is directly related to the twinning activity in nanostructured Ti.

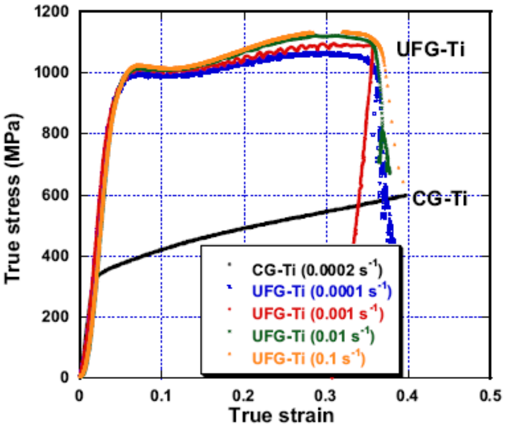

Fig. 1 Room temperature compressive true stress-strain curves of nanostructured Ti over strain rate range of 10^{-4} s^{-1}–10^{-1} s^{-1}, in comparison with a representative true stress-strain curve of the coarse-grained Ti.

Reference

Y.M. Wang, J.Y. Huang, T. Jiao, Y.T. Zhu, A.V. Hamza, *J. Mater. Sci.* 42, 1751-1756 (2007).

Control of Macroscopic Strain via Surface Chemistry

A. Wittstock, J. Biener, M. M. Biener, and A. V. Hamza (LLNL),
V. Zielasek, and M. Bäumer (Universität Bremen),
D. Kramer, R.N. Viswanath, and J. Weissmüller (Forschungszentrum Karlsruhe)

Muscles enable humans to do mechanical work by converting chemical energy. The working force of a muscle is generated in ligaments consisting of the proteins actin and myosin. By scission of ATP (adenosine tri phosphate), the biological energy currency, reversible change of conformation of the protein molecules is induced. Simultaneous action of actin/myosin ligaments leads to a macroscopic contraction of a muscle. Can this complex biological system be mimicked?

Inorganic materials such as gold nuggets don't tend to shrink or expand depending on conformational changes at their surface. But nanoporous (np) materials such as metal foams, consisting of a mesh of nano-sized ligaments, have a much higher surface-to-volume ratio.

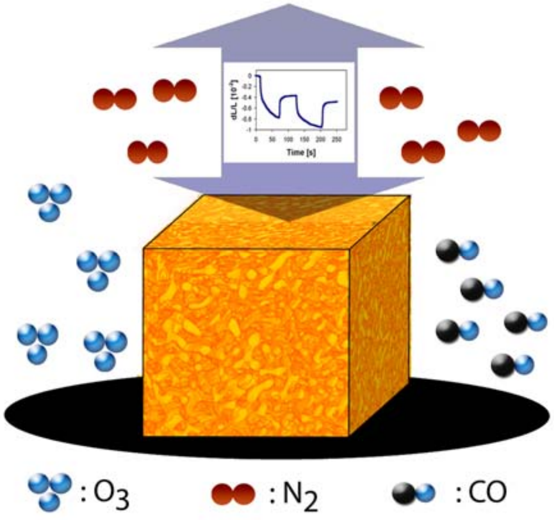

***Fig. 1**: Strain induced by surface chemistry.*

Obviously the mechanical properties of such a material are far more influenced by surface processes. Conformational change at the surface can therefore induce changes in the overall mechanical properties of these materials. Weissmueller at al. [1, 2] showed that changing the conformation of the surface by charging of np gold or platinum leads to strain in the range of up to 0.02 % of the macroscopic dimensions. Therefore we know that charge at the surface induces macroscopic strain.

For our chemo-mechanical approach we use atomic oxygen as an electronegative element which binds to the (gold) surface [3, 4]. Due to the higher electro negativity of the chemisorbed oxygen atoms the gold surface gets positively charged [5].

We prepared cuboids of np-Au by electrochemical dealloying of a Ag75Au25 alloy in perchloric acid with the dimensions of 1x1x1 mm^3 and monitored the strain of the samples in situ with a commercial dilatometer equipped with a small gas chamber for environmental control. As a simple source of atomic oxygen we used ozone which decomposes at the gold surface [6]. For removal of chemisorbed oxygen atoms from the surface we used carbon monoxide in analogy to heterogeneous catalysis [7, 8].

First we combined the oxidation step and the reduction step into cycles of different length. Thus, we triggered the conformational change of the gold surface (*Fig. 2*). The oxidation step was accompanied by a fast contraction of the material, whereas during reduction the material expanded nearly to its original length. We observed a background-shrinking of the material which became more and more evanescent after a few cycles of oxidation and reduction. This behavior was likely influenced by an over all stress relief of the material after dealloying. However, the contraction-/expansion amplitude during cycles lasting about two hours was approximately 0.5 % of the edge length of the cuboid (*Fig. 2*, A). An amazing high amplitude considering that commercially piezoelectric materials have strain amplitudes of about one twentieth of this value. We also observed black staining during oxidation, it was reversibly switched to a golden color during reduction which is a visual indication of the interaction of the np-Au with the surrounding gases and reversible manipulation of the surface configuration.

Speeding up the succession of contraction and expansion is shown in Part B of *Fig. 2*. We cycled the oxidation and reduction in a time frame of a couple of minutes (here 5 minutes), but no remarkable changes in strain amplitudes where detectable.

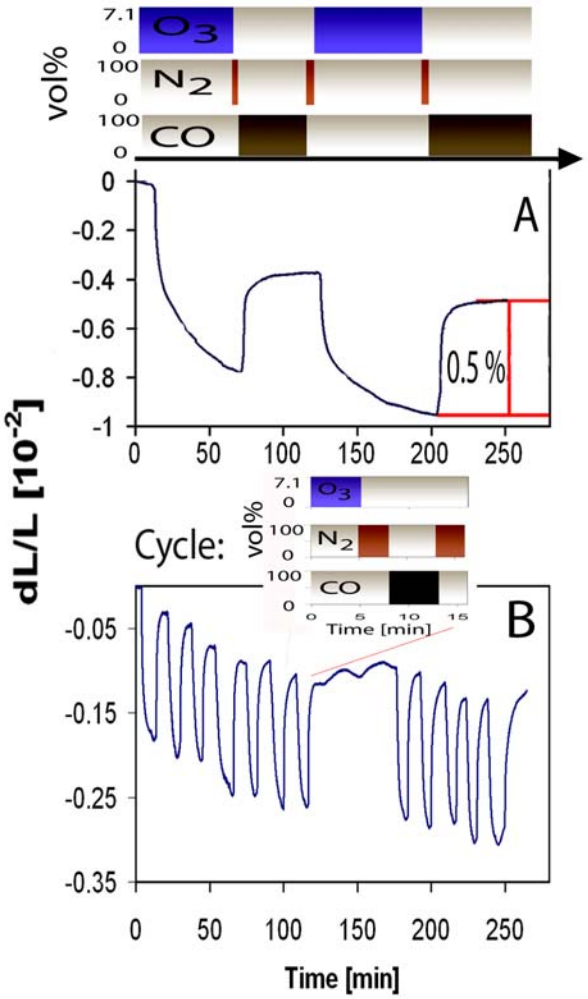

Fig. 2: *Dependence of the edge length (L = 1 mm) of a cubic np-Au sponge on the ambient gas. To prevent heat production due to direct reaction of CO with O_3 each gas was carefully removed (purge gas N_2) before switching. (A) Strain (contraction and expansion) during oxidation and reduction cycles each lasting about two hours. (B) Short-time cycling of contraction and expansion.*

Variation of the concentration of ambient ozone lead to variation of compression amplitudes, whereas the amplitude increased with increasing ozone concentration (*Fig. 3*). This is not amazing since the coverage of the gold surface with oxygen depends on the decomposition of ozone. But proves the direct relation between the surrounding gas and the conformation of the surface.

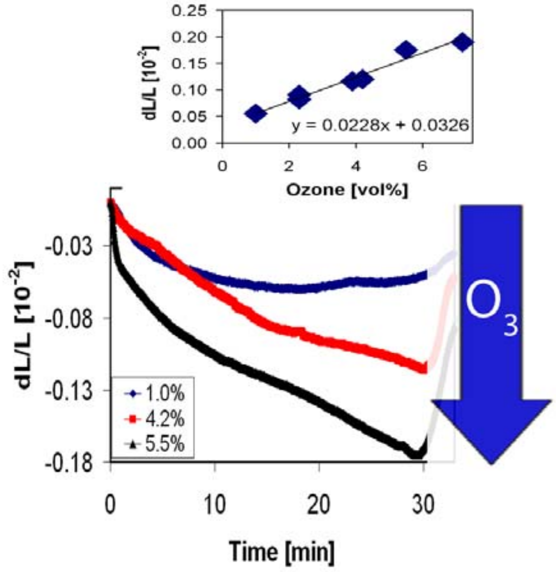

Fig. 3: *Dependence of compression amplitude on the concentration of ambient ozone. In the lower chart three different curves of compression vs. time are plotted for different ozone concentrations. The upper charts displays the compression amplitude depending on the particular ozone concentration after 30 minutes of exposure.*

Changes in conformation lead to macroscopic strain, in biological systems as well as in inorganic systems. We show that this is only a matter of size. Due to the small ligaments of the np-Au foam we can contract and enlarge them by influencing the conformation of the surface by chemisorbed atomic oxygen. Since we convert chemical energy directly into mechanical work our system is a mimic muscle, though with a much smaller efficiency than a biological muscle, yet.

References:

1. Weissmuller, J., et al., Science, 2003. **300**(5617): p. 312-315.
2. Kramer, D., R.N. Viswanath, and J. Weissmuller, Nano Letters, 2004. **4**(5): p. 793-796.
3. Kirn, J., E. Samano, and B.E. Koel, Surface Science, 2006. **600**(19): p. 4622-4632.
4. Min, B.K., et al., Physical Review B, 2005. **72**(12).
5. Torres, D., K.M. Neyman, and F. Illas, Chemical Physics Letters, 2006. **429**(1-3): p. 86-90.
6. Hao, Z.P., et al., Applied Catalysis B-Environmental, 2001. **33**(3): p. 217-222.
7. Jurgens, B., et al., Gold Bulletin, 2007. **40**(2): p. 142-149.
8. Zielasek, V., et al., Angewandte Chemie-International Edition, 2006. **45**(48): p. 8241-8244.

Synthesis of nanoporous TiO_2 foam using template based atomic layer deposition

S. Ghosal, T. F. Baumann, J. Biener, S. O. Kucheyev, Y.-M. Wang, M. A. Worsley, A. V. Hamza(LLNL)
J. S. King and S. F. Bent (Stanford University)

Titanium dioxide (TiO_2) is a technologically important wide band-gap transition metal oxide with numerous applications in areas such as heterogeneous catalysis, solar cells, optical and corrosion coatings, to name just a few. In recent years, synthesis and properties of nanostructured TiO_2 have attracted considerable interest. However, most of the research efforts have been focused on titania nanoparticles and nanopowders [1]. The NSCL group has previously reported the synthesis and characterization of a rather extreme form of nanoporous titania - low density TiO_2 aerogels which are typically characterized by a high degree of porosity, with ultrafine (nanometer size) cells/pores [2, 3]. These TiO_2 aerogels were derived via sol-gel synthesis. Another possible synthetic route to nanoporous titania is through TiO_2 atomic layer deposition (ALD) onto a nanoporous template. The template approach offers control over the composition and morphology of the resulting structure and thus can be used to introduce desired structural features. Also, the ALD process which uses a pair of sequential, self-limiting surface reactions, offers excellent atomic level control of the deposited film thickness and uniformity.

We used a low density silica aerogel (~10 mg/cm^3) as a template for the synthesis of nanoporous titania. TiO_2 films were deposited onto the template via ALD process involving alternating exposures to titanium tetrachloride ($TiCl_4$) and water at 100º C. Rutherford back scattering measurements show uniform deposition of titania with depth into the aerogel. High resolution TEM images of the aerogel template following ALD show the presence of TiO_2 nanoparticles (Fig.1). It is evident from selected-area diffraction pattern of a nanoparticle (Fig. 1a, inset) that the deposited titania is of crystalline rutile phase and not amorphous as would be expected. The growth of rutile phase titania requires significantly higher temperature than 100º C. Therefore, a possible explanation for the growth of rutile titania via ALD is that the temperature within the aerogel during deposition was higher than expected, thereby leading to a reaction pathway for the formation of rutile titania. Aerogels are excellent insulators due to their highly porous morphology. Hence, if there is sufficient heat generated during the TiO_2 ALD process, it could result in temperature rise at the reaction site due to poor dissipation of heat through the aerogel. Experiments are currently underway to monitor temperature within the aerogel during ALD. Preliminary measurements show rise in temperature above the set point during the growth process. Accurate knowledge of growth conditions during the ALD process is essential for regulating structure and composition of the deposited film and thereby controlling its properties.

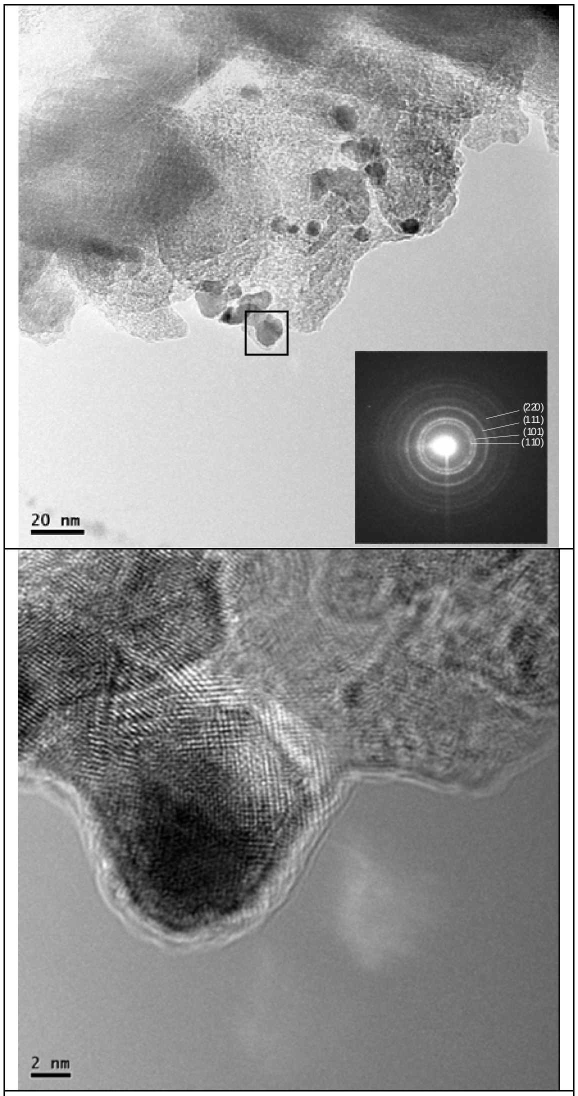

Fig.1. High-resolution TEM images of aerogel post TiO_2 ALD. The inset in (a) shows selected area diffraction pattern of deposited TiO_2 nanoparticle. (b) Single-crystalline rutile nanoparticle highlighted by the box in (a).

References

1. U. Diebold, Surf. Sci. Rep. 48 (2003) 53.

2. S.O. Kucheyev, T. van Buuren, T.F. Baumann, J.H. Satcher Jr., T.M. Willey, R.W. Meulenberg, T.E. Felter, J.F. Poco, S.A. Gammon, L.J. Terminello, Phys. Rev. B 69 (2004) 245102.

3. S.O. Kucheyev, T.F. Baumann, Y.M. Wang, T. vanBuuren, J.H. Satcher Jr, J. Electr. Spectr. Rel. Phenom. 144-147 (2005) 609.

A new platinum catalyst: ALD coated carbon aerogels

A. Wittstock, J. Biener, T. F. Baumann, S. O. Kucheyev, Y. M. Wang, and A.V. Hamza (LLNL),
M. Bäumer, and V. Zielasek (Universität Bremen),
J.S. King, and S.F. Bent (Stanford University)

Heterogeneous catalysis has an enormous impact on chemical industry. During the manufacture of about 90 percent of all chemicals heterogeneous catalysts are involved. The world market for catalysts counts about US $10 billion and is still increasing. New strategies for the preparation of catalysts is the key for achieving higher activity, selectivity, and durability, which will lead to a higher productivity. Furthermore, improved catalysts reduce the impact on the environment and thus contribute to a green and sustainable chemistry. An important class of heterogeneous catalysts are supported metal particles. As the particle size is one of the key factors determining catalytic activity and selectivity, a major task is the preparation of catalysts with predefined particle sizes.

Here, we show that highly reactive aerogel/Platinum nanoparticles hybrid materials can be obtained by atomic layer deposition (ALD). The ALD approach results in the deposition of monodisperse, highly reactive Pt nanoparticles.

As support, carbon aerogels were used. This material is also a promising candidate for hydrogen storage [1]. It can be easily and inexpensively produced in a large variety of sizes and forms with an adjustable specific surface area. Monolithic pieces, although exhibiting a low density (~0.5 g/cc), are still mechanically robust (modulus of up to 3 GPa). Another interesting property in the context of high-surface-to-volume electrode materials is their electrical conductivity.

Platinum group metals (Pt, Ir, Rh and Pd) are known to be very good catalysts for the oxidation of carbon monoxide. Although being a comparatively simple reaction that was intensively investigated already in the past, there is rising interest in the oxidation of CO due to its importance in pollution control, the industrial and automobile exhaust cleaning. Here we use this mechanically relatively simple reaction as a test reaction. We will show that the preparation of aerogels and subsequent atomic layer deposition is a suitable way to prepare CO oxidation catalysts with well defined structural properties.

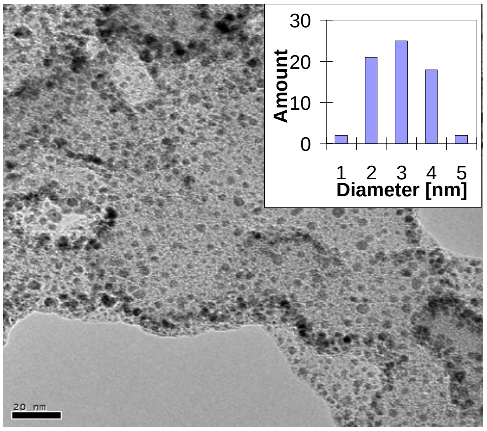

Fig. 1: Transmission electron micrograph of a FIB-liftout of a carbon aerogel (10 cycles ALD). The observed spot is approx. 5 µm below the exterior surface. Inset: Platinum particle size distribution.

Carbon aerogels were loaded by atomic layer deposition with different amounts of platinum (2, 5, and 10 cycles of ALD). The resulting Pt concentration was analyzed by Rutherford backscattering spectroscopy (RBS, see *Fig. 2*). For the sample coated with 10 cycles of Platinum the distribution of particles on the support and their sizes were determined by transmission electron microscopy (*Fig. 1*). The average particle diameter is about 3 nanometer with a standard deviation of less than a nanometer. The particles are well distributed over the surface of the aerogel. However, the TEM-data reveal a variation of particle sizes when moving from the outer surface to the inner sections of the aerogel. For higher loadings (10 cycles of ALD), we observe a rapid decrease of the particle diameters within the first 3 microns below the outer surface. Going deeper, the particle diameter remains nearly constant, while the number density decreases. These results are in good accordance with data obtained by Rutherford backscattering spectroscopy (RBS).The gradient is likely induced by a limited mass transport through the narrow capillaries of the aerogel.

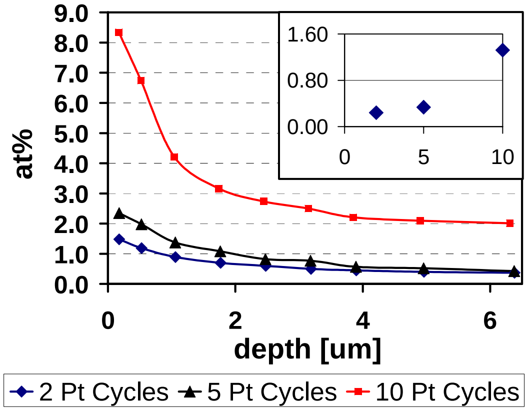

Fig. 2: Depth profile of Platinum loading. Investigated by Rutherford backscattering spectroscopy (RBS). Inset: Total amount of Pt [10^{-7} mol/cm^2] versus cycles of Pt ALD.

The catalytic properties of all samples were investigated in a continuous flow reactor. The obtained conversion rates and a scheme of the reactor are shown in *Fig. 3*.

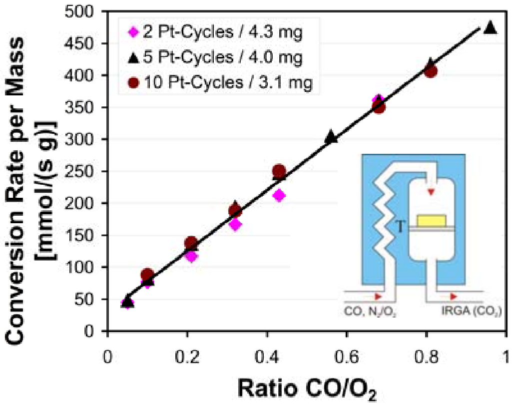

Fig. 3: Conversion rates referred to the particular mass of catalyst. The amount of produced CO_2 at the reactor outlet was detected by an IR-analyzer. ($T_{reactor}$=200 °C, synth. air 80/20 vol% N_2/O_2, CO 4.7, supply Linde AG).

Comparison of the differently coated aerogels shows that already two cycles of ALD are sufficient to generate a highly active catalyst. Based on TEM and RBS data we calculated the averaged total platinum surface. Assuming that only the outer 10 microns of the aerogel are coated with platinum, and that the particles have a hemispherical morphology, results in a turn-over-frequency (TOF) of about 29 s^{-1}. This value is in agreement with model experiments [2] and proves that a highly active catalyst can be obtained by only 2 cycles of ALD resulting in very low Pt loading levels. Due to a limited mass transport through the narrow pores of the aerogel, a further loading of platinum does not lead to an increase in activity. Indeed, the Pt aerogel hybrid marerial is so reactive that the heat production at elevated conversion rates induces a irreversible destruction of catalyst by combustion of the carbon aerogel.

We conclude that carbon aerogels coated with platinum by ALD are highly active catalysts for the oxidation of carbon monoxide. Due to the wide range of possible combinations of substrates and metal coatings by ALD, this is a promising strategy to generate a new class of catalysts and a very interesting application of surface engineering.

1. Kabbour, H., et al., *Towards New Candidates for Hydrogen Storage: High-Surface-Area Carbon Aerogels.* Chemistry of Materials, 2006. **18**(26).
2. Santra, A.K. and D.W. Goodman, *Catalytic oxidation of CO by platinum group metals: from ultrahigh vacuum to elevated pressures.* Electrochimica Acta, 2002. **47**(22-23): p. 3595-3609.

Mechanisms of atomic layer deposition on substrates with ultrahigh aspect ratios

S. O. Kucheyev, J. Biener, T. F. Baumann, Y. M. Wang, A. V. Hamza (LLNL), Z. Li, D. K. Lee, and R. G. Gordon (Harvard University)

Technological applications of nanoporous solids, directly related to their large surface areas or low densities, are numerous. However, mature synthesis technologies, with flexibility and control over material properties, have been developed for only a limited number of nanoporous systems, such as porous polymers, sol-gel-derived silica, alumina, and zeolites. It is, therefore, highly attractive to develop a tool for uniform coating of the inner surfaces of the existing robust nanoporous systems with control over the elemental composition, thickness, and morphology of the coating. Unfortunately, the ultra-high effective aspect ratios inherent to bulk nanoporous solids severely limit the usefulness of most deposition techniques, such as physical vapor deposition and non-self-limiting versions of chemical vapor deposition.

Atomic layer deposition (ALD) appears to be uniquely suited for coating substrates with ultrahigh aspect ratios ($>10^3$), including nanoporous solids. In this project [1], we have studied the mechanisms and address current challenges of ALD on nanoporous monoliths with typical effective aspect ratios $>10^3$. In particular, we have studied ALD of Cu and Cu_3N on the inner surfaces of low-density nanoporous silica aerogels. Results have shown that Cu depth profiles in nanoporous monoliths are limited not only by Knudsen diffusion of heavier precursor molecules into the pores, as currently believed, but also by other processes such as the interaction of precursor and reaction product molecules with pore walls. Similar behavior has also been observed for Fe, Ru, and Pt ALD on aerogels. In addition, this study shows that the precursors and process parameters developed for successful ALD on substrates with moderate aspect ratios ($<10^3$) could have limited suitability for coating bulk nanoporous solids. Much more volatile precursors will likely be needed for ALD on substrates with ultrahigh aspect ratios.

Reference

[1] S. O. Kucheyev, J. Biener, T. F. Baumann, Y. M. Wang, A. V. Hamza, Z. Li, D. K. Lee, and R. G. Gordon, Langmuir **24**, 943 (2008)

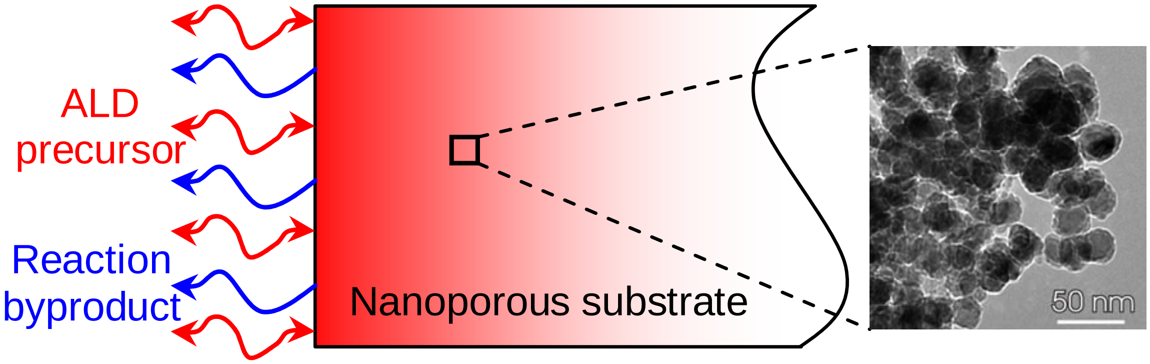

Figure 1.: Schematic illustration of ALD on nanoporous substrates

Electronic structure of nanoporous ceria

S. O. Kucheyev, B. J. Clapsaddle, Y. M. Wang, T. van Buuren, and A. V. Hamza

Cerium compounds are the best studied rare-earths due to their technological importance and the interesting physical properties inherent to the f-electron systems. Recently, there have been numerous reports on nanostructured cerium oxides, with a major focus on an increase in the surface area to boost their catalytic efficiency. One approach to the synthesis of nanostructured ceria is the sol-gel process. Several recipes for sol-gel-derived ceria nanomaterials, and aerogels (AGs) in particular, have been reported. Such AGs are open-cell nanoporous solids derived from highly cross-linked wet gels by drying them under supercritical conditions. However, the technologically important electronic structure of sol-gel-derived nanoporous ceria remains essentially unexplored.

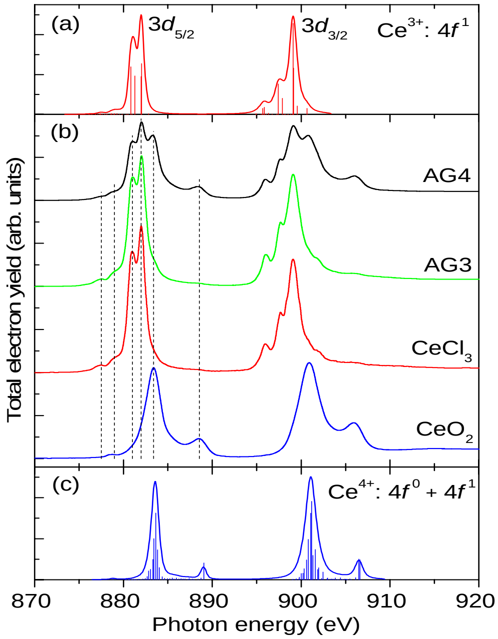

Figure 1.: Cerium $M_{4,5}$-edge XANES spectra for two representative ceria aerogels (labeled AG3 and AG4) and reference compounds. Experimental data are shown in (b) and results of atomic multiplet calculations for Ce^{3+} and Ce^{4+} in (a) and (c), respectively

As we discussed in more detail in [1], we have studied the electronic structure of three-dimensional nanoporous CeO_{2-x} monoliths (AGs) by soft x-ray absorption near-edge structure (XANES) spectroscopy. Atomic multiplet calculations are used to interpret high-resolution Ce $M_{4,5}$- and $N_{4,5}$-edge XANES spectra. Figure shows Ce $M_{4,5}$-edge XANES spectra of two representative AGs and of full-density reference materials. Results show that aerogels with thicker ligaments, but with the same average size of crystallites, exhibit larger Ce^{3+} content and, hence, higher oxygen deficiency. This finding has been attributed to a larger concentration of O vacancies in crystallites in AGs with thicker ligaments. Our study have also shown that the electronic structure of sol-gel-derived nanoporous ceria strongly depends on preparation conditions, and more work is currently needed to gain a better control of the properties of ceria AGs in order for their technological potential to be fully exploited.

Reference

[1] S. O. Kucheyev, B. J. Clapsaddle, Y. M. Wang, T. van Buuren, and A. V. Hamza, Phys. Rev. B. **76** 235420 (2007).

Electronic structure of chromia aerogels

S. O. Kucheyev, B. Sadigh, T. F. Baumann, Y. M. Wang, T. E. Felter, T. van Buuren, A. E. Gash, J. H. Satcher, Jr., and A. V. Hamza

Numerous approaches to the synthesis of high-surface-area chromia, and chromia aerogels (AGs) in particular, have been reported. Such AGs are an extreme form of high-surface-area nanomaterials. However, no information about the surface electronic structure, which is crucial for the performance of AGs as catalysts, has been reported. Moreover, we are not aware of any previous electronic structure studies of nanostructured chromia. In this work, we have synthesized and studied the electronic structure of high-surface area chromia AGs. The main results of this work, discussed in detail in [1], can be summarized as follows.

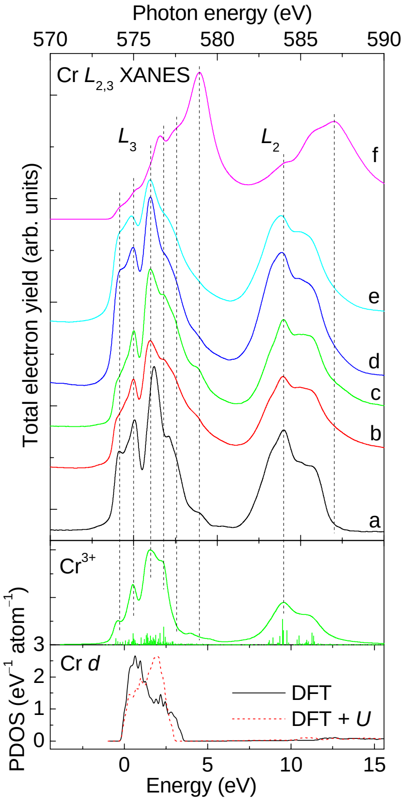

Figure 1: Top panel: Chromium L-edge XANES spectra of (a) an as-synthesized aerogel, (b) an aerogel annealed at 550 C, (c) alpha-Cr_2O_3 powder, (d) an alpha-Cr_2O_3 single crystal, (e) full-density amorphous Cr_2O_3, and (f) CrO_3. Middle panel: Crystal field multiplet calculations. Bottom panel: PDOS in bulk alpha-Cr_2O_3.

(i) We have presented high-resolution O K-edge and Cr L-edge (see figure) x-ray absorption near-edge structure (XANES) spectra of nanostructured chromia AGs, alpha-Cr_2O_3, orthorhombic CrO_3, and amorphous Cr_2O_3.

(ii) The electronic structure of bulk alpha-Cr_2O_3 has been calculated with DFT and DFT+U.

(iii) The structure of the valence band and the O-related unoccupied states of alpha-Cr_2O_3 are better described with our DFT rather than DFT+U calculations.

(iv) Both O K-edge and Cr L-edge XANES spectra of as-prepared aerogels are significantly different from those of bulk alpha-Cr_2O_3, CrO_3, or amorphous Cr_2O_3. For the O K edge, this difference is attributed largely to the presence of O-containing impurities (the expected hydration, in particular). For the Cr L edge, it is attributed to different symmetry and strength of the crystal field for fully coordinated bulk Cr atoms and surface atoms.

(v) Spectra of thermally treated aerogels exhibit additional peaks (at ~528.0 and ~579.0 eV), attributed to the presence of Cr VI species.

(vi) As compared to the case of alpha-Cr_2O_3, spectra of amorphous Cr_2O_3 are shifted by ~0.4 eV and ~0.1 eV to lower energies for O K and Cr L edges, respectively.

(vii) Thermal treatment transforms as-prepared amorphous aerogels into alpha-Cr_2O_3 nanopowders.

Reference

[1] S. O. Kucheyev, B. Sadigh, T. F. Baumann, Y. M. Wang, T. E. Felter, T. van Buuren, A. E. Gash, J. H. Satcher, Jr., and A. V. Hamza, J. Appl. Phys. 101, 124315 (2007).

Bonding Low-density Nanoporous Metal Foam to an Aluminum Foil

Matt Bono, Octavio Cervantes, Ron Forman

A method has been developed for bonding low-density nanoporous metal foam components to a substrate using solder that is sputtered onto the surfaces. Copper foam equation-of-state laser experiments drive a shockwave through an aluminum foil and into a copper foam, in order to determine the speed of the shock in the copper foam. To avoid disturbing the shock, the interface between the copper foam and the aluminum substrate must be as thin as possible. Achieving a sufficiently thin bond is challenging, because traditional liquid adhesives would be absorbed into the foam. Here, using sputter-deposited solder, a bond thickness of <2 μm was achieved.

The nanoporous copper foam material was synthesized with a filter casting method that used commercially available copper nanoparticles with diameters of 10-70 nm and 1 μm diameter polystyrene spheres. The filter casting process produced a billet of 20% dense copper foam material approximately 3 mm thick, as shown on the left side of Figure 1. Using a diamond turning process, this billet was machined to a flat disk of thickness 0.5 mm and diameter 3.75 mm, as shown in the center of Figure 1.

Using a razor blade, the foam material was cut into 1 × 1 mm squares with a thickness of 0.5 mm, as shown on the right side of Figure 1. The square was then bonded to an aluminum foil of thickness 38 μm using an indium-based solder that was deposited on the materials using sputtering. A special gripper was fabricated to pick up the 1 mm foam square, hold it upside down in the sputtering system during deposition, move it to the assembly area, and place it during assembly. After coating both the foam and the aluminum foil with 0.7 μm of solder, they were placed into an assembly fixture with the coated surfaces facing each other. A weighted arm pressed the components together as the assembly fixture was placed into an oven to heat the parts and melt the solder. The bonded assembly was then mounted back on the precision lathe to cut the foam to a thickness of 30 μm.

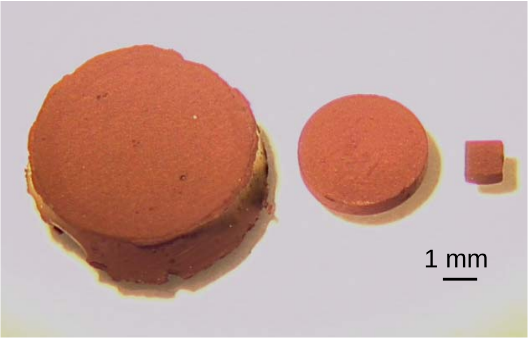

Figure 1. Copper foam material cast in the synthesis process (left), diamond turned to a disk (center), and cut into a 1×1 mm square (right)

One of the parts was placed in a focused ion beam system, which machined a cross-section into the material to expose the interface, as shown in Figure 2. The solder is evident between the foam and the substrate, and the two layers of solder that had been deposited on the individual components have melted together to form a single layer with a thickness of approximately 1.5 μm. The solder did not wick into the foam to any significant extent, and there are no voids in the foam at the interface larger than a few μm.

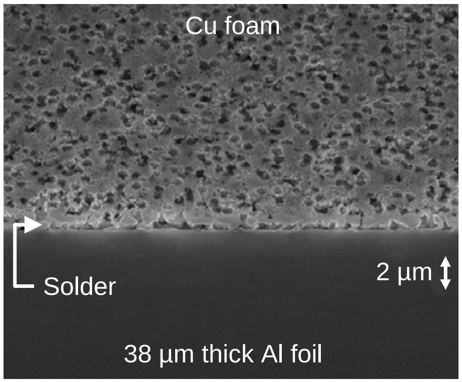

Figure 2. SEM image of the bonded interface between the copper foam and the aluminum foil

Structure of low-density nanoporous dielectrics revealed by low-vacuum electron microscopy and small-angle x-ray scattering

S. O. Kucheyev, T. F. Baumann, A. V. Hamza, C. K. Saw, T. van Buuren, Y. M. Wang, T. M. Willey (LLNL),
M. Toth, W. R. Knowles (FEI Co.), J. Ilavsky (Argonne National Laboratory), B. L. Thiel, V. Tileli (SUNY Albany)

Aerogels (AGs) are a class of ultralow-density open-cell nanoporous solids with typical porosities of >90% and large surface areas. Aerogels often display vastly different nanoligament shapes and sizes, including near spherical particles, rods with different aspect ratios, and quasi-two-dimensional (2D) leaflets. The shape and size of ligaments in nanoporous dielectrics are commonly studied by transmission electron microscopy (TEM). However, technologically important properties of nanoporous solids strongly depend not only on the ligament structure but also on the distribution of ligament and pore sizes (i.e., density fluctuations) and the presence of other structural inhomogeneities such as microcracks. Conventional TEM imaging does not probe such information.

Other techniques commonly used to image dielectric nanomaterials are scanning electron (SEM) and atomic force (AFM) microscopy. These methods, however, face serious challenges in the case of low-density nanoporous dielectrics. Consequently, AG morphology is commonly studied by indirect methods such as nitrogen sorption and small-angle x-ray (SAXS) and neutron (SANS) scattering. However, as we discuss in [1], information obtained from nitrogen sorption is limited, and real-space interpretation of SAXS and SANS data from complex nanoporous systems is highly model dependent.

In this project, we demonstrate unambiguous visualization of the structure of several representative highly-insulating AGs over a wide range of length scales (~10^0 – 10^5 nm). We use low-vacuum SEM (LVSEM), where charging is stabilized by a small amount (<100 Pa) of weakly ionized gas inside the specimen chamber. In particular, our results reveal the presence of large-scale pores (i.e., hundreds of nanometers in size, see the figure) in some AGs and the existence of a highly-defective skin layer on otherwise crack-free monoliths for all the AGs studied. These features cannot be studied by the abovementioned techniques and have important implications for understanding AG properties affecting their mechanical, gas/fluid diffusion, adsorption, optical, and electronic transport behavior. We use the LVSEM results to interpret SAXS curves for these complex nanoporous systems. The methodology presented by us in [1] is very efficient and is expected to play a central role in future work on synthesis and functionalization of nanoporous dielectrics.

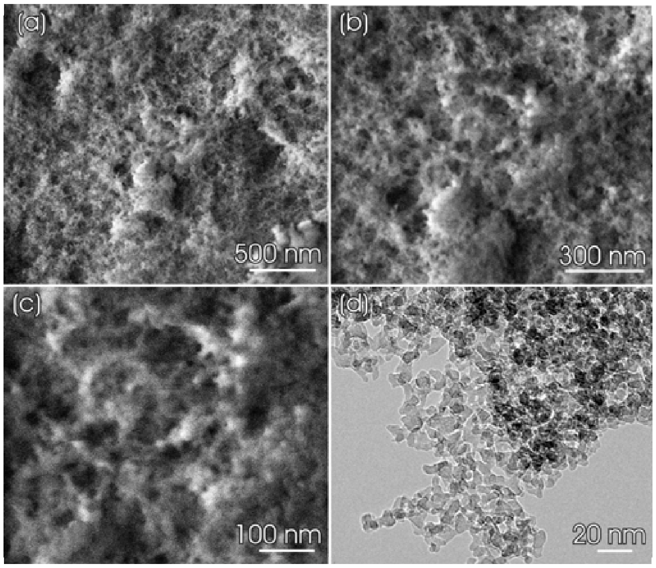

Caption: Low-vacuum SEM (a-c) and conventional bright-field TEM (d) images of a cross-section of the alpha-AlOOH aerogel.

Reference

[1] S. O. Kucheyev, M. Toth, T. F. Baumann, A. V. Hamza, J. Ilavsky, W. R. Knowles, C. K. Saw, B. L. Thiel, V. Tileli, T. van Buuren, Y. M. Wang, and T. M. Willey, Langmuir **23**, 353 (2007).

Synthesis and Characterization of Low Density Copper and Palladium Foams

Gregory W. Nyce, Alex V. Hamza, and Joe Satcher Jr.

Templating and casting are two approaches to incorporate and control porosity within metals [1]. Templating uses sacrificial inorganic or organic materials to generate pore sizes ranging from the nanometer to the micron scale. In addition, the casting process incorporates porosity into a material by virtue of the interparticle spacing between packed particles.

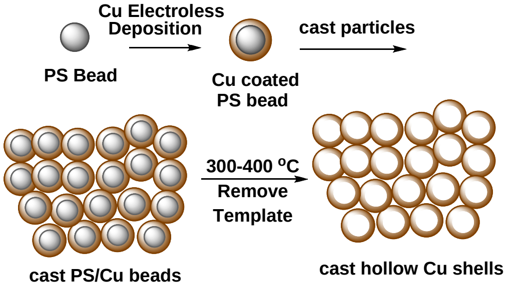

Scheme 1. Synthesis of low density copper monoliths

To prepare low density copper matierals, our strategy was to cast prepare templated hollow copper shells that could be prepared in monolithic pieces, Scheme 1. We adopted a core-shell approach to prepare the hollow Cu shells [2]. Initially we chose polystyrene (PS) beads as templates since they are easily prepared or commercially available. To prepare the PS template for Cu electroless deposition the template surface was treated with gold nanoparticles that act as seeding sites for Cu deposition. Cu electroless deposition on PS proceeded smoothly and then the Cu/PS beads were cast into a monolith, Scheme 2.

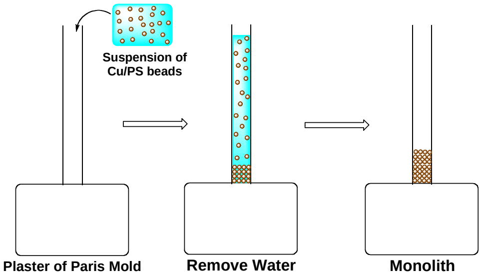

Scheme 2. Casting Cu/PS beads

The casting procedure is analogous to slip-casting of ceramic and metal particles in which a suspension of PS/Cu particles is placed in a plaster of paris mold and allowed to settle. The plaster of paris is a deposition surface for the particles and slowly removes water from the suspension to create a dry monolith.Heating the Cu/PS monoliths to 400 °C under N_2 removed the PS template leaving a copper monolith. SEM analysis of the cooper monolith shows a microstructure mostly comprised of collapsed shells, Figure 1.

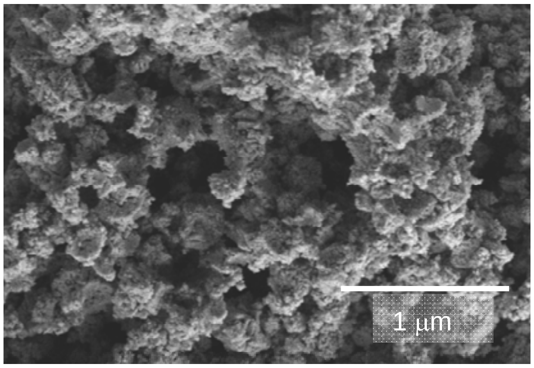

Figure 1. SEM image of collapsed Cu microstructure after PS bead bakeout

The collapse is likely due to the high rate of diffusion of copper at elevated temperatures. Lowering the temperature was not effective since it consistently resulted in incomplete PS bakeout. In in effort to minimize the collapse of Cu shells within the copper microstructure we turned to alternative templates that have a lower decomposition temperature. We became interested in polyalphamethylstyrene (PAMS) as a template candidate due to its superior thermal decomposition properties relative to PS. For example, under an inert atmosphere at 300 °C, PAMS is completely removed. Unfortunately, microspheres of PAMS are not commercially available and are not readily synthesized in the laboratory. We were able to prepare PAMS microspheres using emulsion techniques by carefully mixing PAMS polymer and emulsifier in water/oil using a centrifugal mixer. Once the PAMS microspheres were prepared Cu/PAMS core shell particles were prepared by Cu electroless deposition. The Cu/PAMS particles were cast and heated to 300 °C for 4h to yield a copper foam. SEM analysis of the copper foam microstructure shows minimal collapse of the Cu hollow shells, Figure 2. Large monolithic pieces (mm^3) are readily achieved and are only limited by the size of the tube and quantity of material. The densities of the copper monoliths were measured to be 700 – 800 mg/cc (8-9 % relative density). These techniques are easily extended to other metals in the periodic table and we have used analgous techniques to prepare low density foams of palladium metal. Using PS or PAMS templates, Pd foams with 10% relative density were prepared, Figure 2.

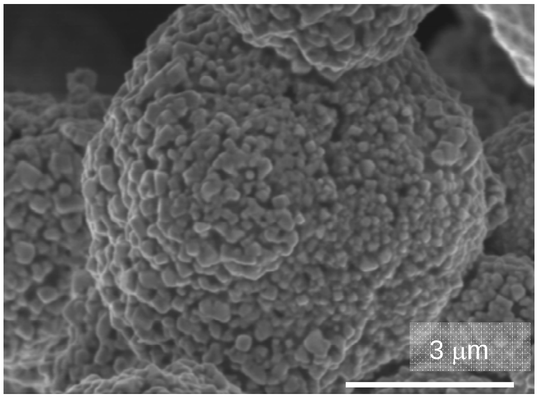

Figure 2. SEM image of nanoporous Cu hollow shell prepared from Cu/PAMS particles

We have synthesized low density nanoporous Cu and Pd monoliths using a novel approach of casting and templating. Monolithic catalysts are of interest as alternatives to traditional powder/slurry systems due to catalyst reusability and minimization of environmental waste. The catalytic oxidation activity as well as the mechanical strength properties of these materials are currently under investigation.

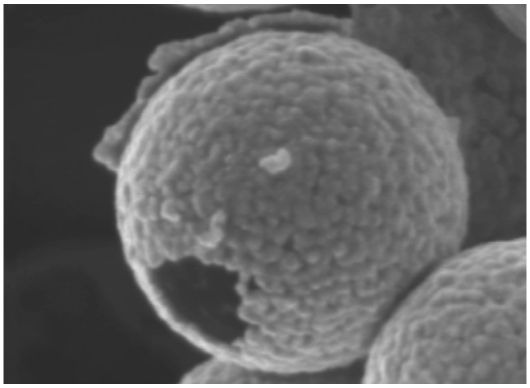

Figure 3. SEM image of nanoporous Pd hollow shell in as prepared low density Pd monolith. Shell thickness is estimated at 35 nm.

References

[1] (a) Stein, A. *Adv. Mater*. **2003**, *15*, 763. (b) Schüth, F. *Chem. Mater*. **2001**, *13*, 3184. (c) Sanchez, C.; Lebeau, B.; Chaput, F.; Boilot, J. P. *Adv. Mater*. **2003**, *15*, 1969. (d) Bond, G. C.; Thompson, D. T. *Catal. Rev. Sci. Eng*. **1999**, *41*, 319. (e) van Noort, D.; Mandenius, C. F. *Biosens. Bioelectron*. **1999**, *15*, 203.

[2] Nyce, G. W.; Hayes, J. R.; Hamza, A. V.; Satcher, J. H. *Chem. Mater*. **2007**, *19*, 344.

Developments in the Machinability of CuO Aerogel Material

Matthew Bono, Greg Nyce, Don Bennett, Joe Satcher

Double Shell targets are currently being designed for shots on NIF as a complementary design to the baseline cryogenic ignition target. The primary advantage of the Double Shell targets is that they are designed to yield ignition when fielded in a room temperature hohlraum, so they do not require cryogenic facilities. One of the designs for the Double Shell targets requires components made of low-density CuO aerogel, which will support the inner fuel-filled shell inside the outer ablator shell. Until recently, formulations for synthesizing CuO aerogel produced material that was too fragile for use in a laser target. This material was formed in billets several millimeters in diameter and several millimeters long, but it was extremely fragile and contained a large number of cracks. The material was so fragile that upon attempting to glue it to a mandrel for machining, it simply crumbled into tiny pieces.

Recently, we have developed a CuO aerogel with a density of 50 mg/cm^3 that is strong enough to withstand handling and can be diamond turned into precise shapes. Cast billets of material have a diameter of approximately 6 mm and a length of 5 mm. Figure 1 depicts one of these billets of material that has been glued to a copper mandrel so that it can be mounted on a diamond turning machine. Using a single point diamond cutting tool, the CuO aerogel has been faced off and machined to a diameter of 2.5 mm, as shown in Figure 2. The development of a sufficiently robust low-density CuO aerogel is a successful first step toward producing a material that meets the requirements for the NIF Double Shell targets. Future work will involve eliminating micro-cracking in the material and improving its machining characteristics to improve the diamond turned surface finish.

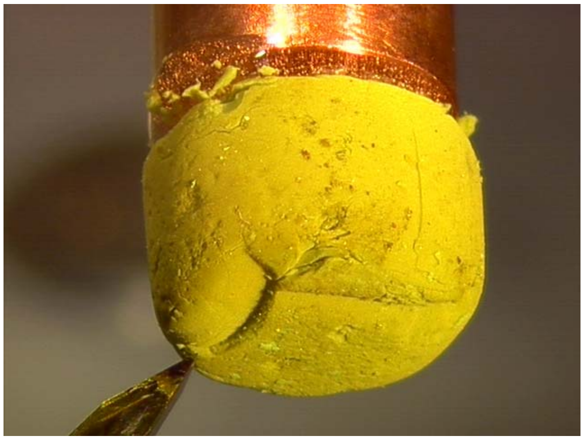

Figure 1. Cast billet of CuO aerogel before being machined

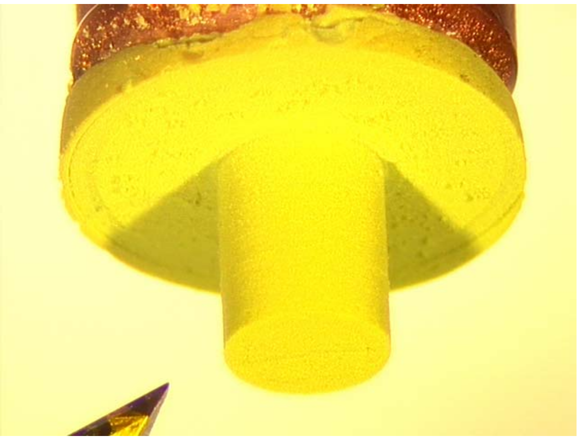

Figure 2. CuO aerogel diamond turned to a cylindrical shape

Mechanical response of free-standing Au nanopillars

Luis A. Zepeda-Ruiz, Babak Sadigh, Juergen Biener, Andrea Hodge and Alex V. Hamza

Size-scale effects in plasticity have attracted much interest as the mechanical properties of nanostructured materials are of great technological importance. As the mechanical behavior of a material relies on defect generation/interaction, one must take into account cases where no internal dislocation sources can be accommodated and surface effects become important.

We use molecular dynamics (MD) simulations to investigate yield mechanisms during compressive deformation of defect-free Au pillars. Our study is based on (001)-oriented nanopillars with realistic cylindrical geometries with aspect ratios of 1:2 in diameter:height. We have worked with highly symmetric nanopillars whose surfaces are covered by steps that delimit mainly two types of facets: (100) and (110). Because of this, the whole surface can be represented by only three types of atoms: (110) terrace atoms, (100) terrace atoms, and step edge atoms.

Figure 1(a) shows the stress-strain curves obtained by applying a 10% compressive deformation to a 20:40 nm freestanding nanopillar at different temperatures. We observe in all cases a linear elastic response for small deformations, followed by a nonlinear elastic regime until the stress reaches a maximum value. At this point of deformation, the system will not be able to sustain any more stress and will start yielding. The yield mechanism is initially purely elastic and thus reversible. However, upon further compression, irreversible plastic deformation occurs by nucleation of <112>{111} partial dislocations at the surface of the nanopillars. With increasing temperature, the systems soften elastically and consequently yield at lower compressions.

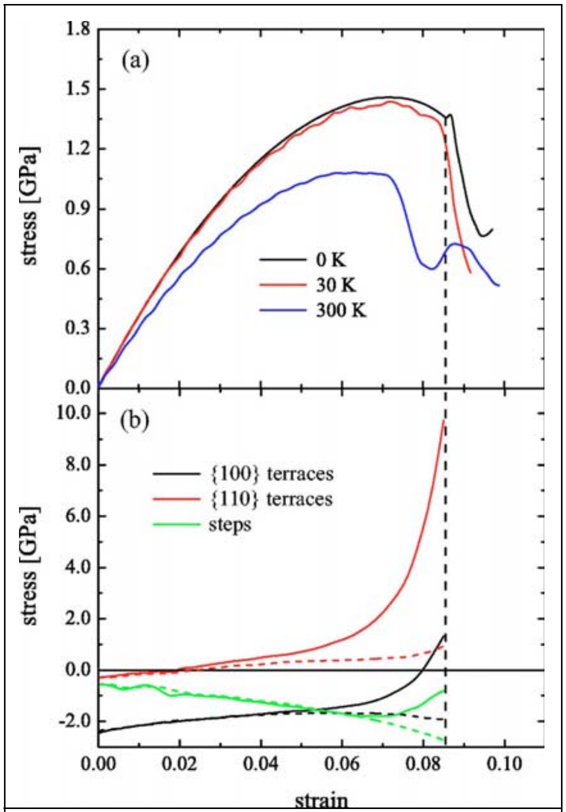

Figure 1. (a) Compressive stress-strain curves for a 20:40 nm freestanding nanopillar at different temperatures. (b) Stress-strain curves for the three types of atoms at the surface of the same nanopillar at 0 K. The solid lines correspond to the surface atoms in the middle region of the cylinder. The dashed curves represent all the surface atoms throughout the entire height of the cylinder. Negative stresses indicate tension.

We have extensively studied the details of the atomistic processes at the onset of plasticity. We find that these processes are highly sensitive to the arrangement of the specific facets on the surface of the cylinders and that different facet orientations can differ dramatically in their response to external stress. Consequently, the onset of plasticity is dictated by how strong each specific surface feature couples to the applied stress. Furthermore, for freestanding nanopillars we find that plasticity is always initiated in their middle region. This is due to a non uniform stress distribution along the height of the cylinders leading to concentration of stress in the center of such nanopillars. This effect is absent when periodic boundary conditions are enforced.

Figure 1(b) shows the stress-strain curves for the three surface atom types mentioned earlier. Solid curves represent the elastic behavior of the surface atoms located in a 2 nm thick region in the middle of the pillar where dislocations nucleate. Dashed curves show the same quantities averaged throughout the entire height of the cylinder. We observe that all the surface atoms are initially under tensile stress (negative values). However, upon compression, the (110) terrace atoms in the center of the cylinder couple strongly to the applied stress and become increasingly compressed. It is important to emphasize that for the specific case of (001)-oriented Au nanopillars chosen for this study, the total stress in Fig. 1(a) decreases beyond the elastic yield point prior to plasticity. This means that in our case the total stress of the system is not necessarily correlated with the onset of plasticity. In addition, the surface stress of the (110) terraces increases monotonically toward the singular point where plasticity is initiated. Hence, the driving force for dislocation nucleation is the compressive stress at the (110) facets.

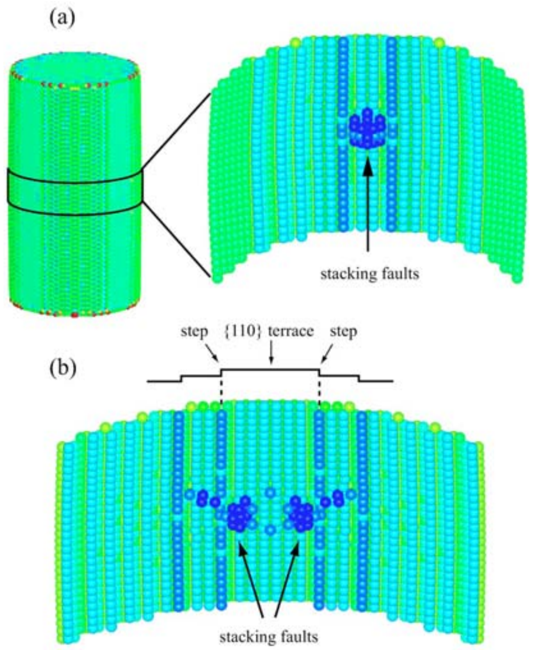

Figure 2. Nucleation of partial dislocations near the step edges for a (a) 10:20 nanopillar and (b) 20:40 nm nanopillar at 0 K.

To further illustrate this point, we show in Fig. 2 the configurations of the middle regions of two nanopillars of different sizes right at the onset of plasticity. We observe that dislocations are nucleated next to the outermost surface layer of the (110) facets close to a step edge.

In conclusion, we have simulated the mechanical response of freestanding Au nanopillars under compressive deformations. We find that the onset of plasticity depends on how strong specific surface features couple to the applied stress. Our simulations show that nucleation of surface dislocations happen near the step edges bounding (110) facets.

Synthesis of Low Density Organic Aerogels

Gregory W. Nyce, Alex V. Hamza, J. Satcher, Jr.

Low density organic aerogels are of interest as new materials for variety of technological applications due to their nanoporous structure and high surface area. Since the introduction of resorcinol/formaldehyde (RF) organic aerogels by Pekala and coworkers at LLNL,[1] there is considerable interest in the synthesis of novel organic aerogels. Most organic aerogels are synthesized by the condensation of an organic molecule with a crosslinker to form a nanoporous 3-D network. We report here the transition metal catalyzed synthesis of a novel organic aerogels.

The aerogels were prepared by ring opening metathesis polymerization (ROMP) by incorporating organometallic ruthenium catalysts (Grubbs catalyst)[2] to suitable monomer solutions. Solutions of dicyclopentadiene (DCPD) are readily polymerized into gels by the addition of Grubbs catalyst, scheme 1. The driving force for the ROMP reaction is release of ring strain energy in the bicyclic DCPD monomer. ROMP is rapid, exothermic, and can result in DCPD gels in a few minutes. The organic solvent in the DCPD wet gels can be extracted using supercritical CO_2 (T_c = 31.1 °C, P_c = 7.4 Mpa) that replaces the solvent with air while leaving the DCPD microstructure unperturbed.

Addition of Grubbs catalyst (2 %) to a solution of DCPD in toluene or THF affords opaque gels within 5 – 10 min. Monolithic pieces (cm^{-3}) of DCPD aerogel with densities from 30-300 mg/cc were readily synthesized.

After the aerogels were synthesized, the, Brunauer-Emmett-Teller (BET) surface area analysis was performed to measure the surface area and pore size distribution of the DCPD aerogels. High surface areas and nanoporosity were observed in the DCPD aerogels from the BET analysis. For example, a 300 mg/cc DCPD aerogel was measured to have 400 m^2/g surface area and average pore size of 30 nm.[2]

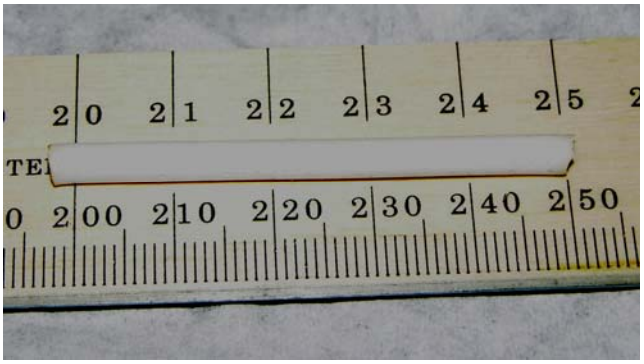

Figure 1. Image of 100 mg/cc DCPD aerogel. 1 cm scale bar.

We have also begun preliminary strength of materials testing of DCPD aerogels using nanoindentation techniques. For example, the compressive strength of a DCPD aerogel (300 mg/cc) was measured to be 11.9 MPa as compared to 66.4 MPa for bulk DCPD.[3]

We have synthesized DCPD aerogels using transition metal catalysis. ROMP of DCPD is s convenient way to obtain low density organic aerogels with high surface area and low porosity. Further work in functionalization of these materials with novel dopents as well additional characterization of the strength of these materials is underway.

References

1. Pekala, R. W.; Schaefer, D. W., *Macromolecules,* **1993,** *26*, 5487.
2. Trnka, T.; Grubbs, R. H. *Acc. Chem. Res.* **2001**, *34*, 18.
3. Constable, G. C.; Lesser, A. J.; Couglin, E. B. *Macromolecules* **2004**, *37*, 1276.

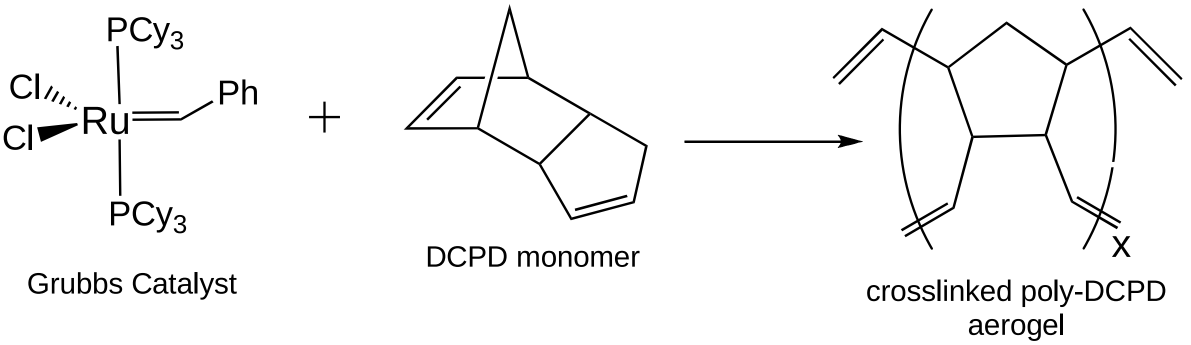

Scheme 1 Synthesis of DCPD aerogel

Nanoparticle Assembly via Electrophoretic Deposition from Aqueous Suspensions

M. A. Worsley, K. Rose, T. F. Baumann, D. Gutierrez, N. Hosannah, P. Buckley, A. V. Hamza

Ordered nanostructured materials have the potential to impact a variety of applications such as microelectronics, photonic devices, energy storage and biosensors. The ability to control the assembly of these materials at the nanometer scale, however, needs further development to allow the full potential of nanostructured materials to be realized. [1]. Towards this goal, we are developing new approaches for the fabrication of ordered nanostructured materials using electrophoretic deposition (EPD). EPD is a process in which charged particles, suspended in a liquid, are deposited via an applied electric field on a substrate of opposite charge. The thickness and morphology of the deposited layer can be readily controlled through the field applied and deposition time [1]. EPD has been used to deposit a wide range of materials including nanoparticles of oxides [2], metals [3], polymers [4], semiconductors [5], and even diamond [6]. While typically been performed in non-aqueous media, recent work has demonstrated that EPD can, at small length scales, be performed using aqueous suspension [7], presenting additional benefits of EPD in terms of cost and environmental impact.

Our goal in this effort is to utilize the EPD process for the fabrication of two general types of ordered nanostructures: 1) gradient density materials and 2) nanocomposites. As a first step in this process, we have demonstrated the ability to deposit thin films of both metal and polymer nanoparticles from aqueous suspensions. For example, as shown in Figure 1, we have used EPD to prepare multilayers of metals through sequential deposition of different-sized gold (Au) nanoparticles. We also extended this approach to deposit up to four layers of different sized polystyrene (PS) beads, as shown in Figure 2. The ability to deposit multiple layers of different sized particles with controlled film thickness can be used to engineer new materials

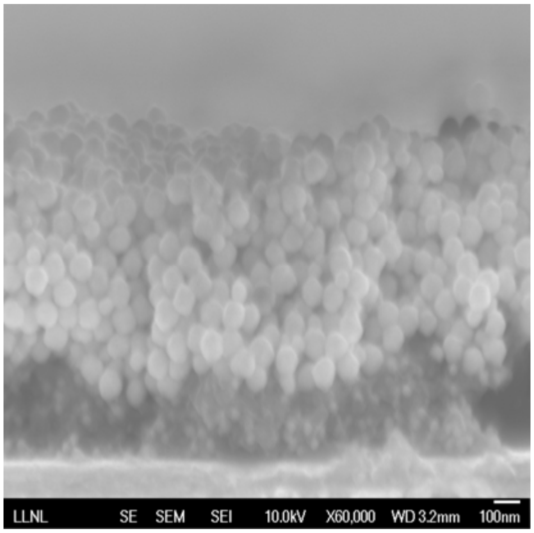

Figure 1. SEM image of a multilayer film consisting of 80nm Au particles deposited on top of a film of 30nm Au particles.

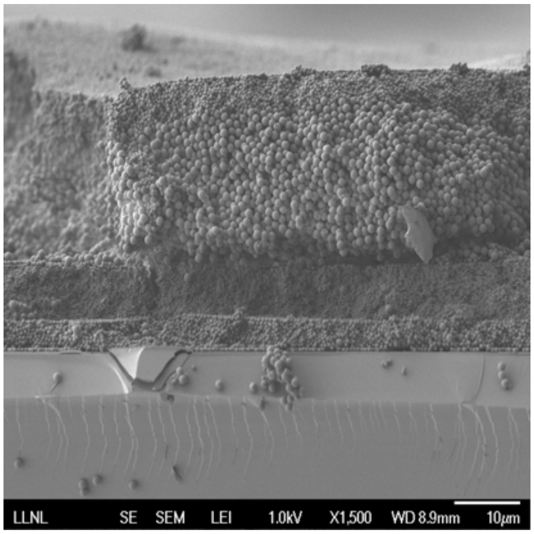

Figure 2. SEM image of a four-layer film consisting of (from top to bottom) 500nm, 1000nm, 200nm and 500nm PS beads.

containing tunable density gradients. In addition to depositing ordered nanostructured materials of a single chemical composition, EPD can also be used to prepare nanocomposites. Just as nanostructured materials have shown exceptional properties compared to bulk materials, nanocomposites can also exhibit properties that exceed those possible with the bulk materials or even macro- and mesoscale mixing. As an example, an EPD composite consisting of both metal (Au) and polymer (PS) nanoparticles is shown in Figure 3.

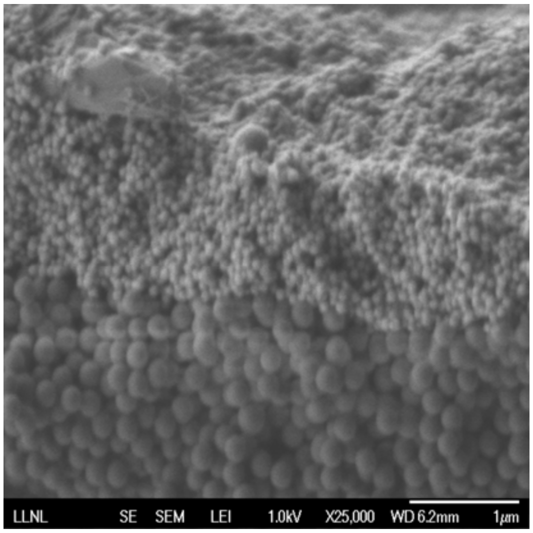

Figure 3. SEM image of a composite film consisting of 80nm Au particles deposited on top of 200nm PS beads.

Electrophoretic deposition promises revolutionary new capabilities in the synthesis of ordered nanostructured materials, but is currently at an early stage of development. As we continue to add to the base of scientific understanding of EPD and identify the relevant factors controlling the growth and ordering of nanostructured materials, we hope to realize the full potential of nanostructured materials.

References

1. Besra, L. and Liu, M., “A review on fundamentals and applications of electrophoretic deposition (EPD),” Progress in Mat. Sci. 52 (2007), 1-61.

2. Kruger, H. G., Knote, A., Schindler, U., Kern, H. and Boccaccini, A. R., J. Mat. Sci. 39 (2004), 839-844.

3. (a) Li, H. X., Lin, M. Z., and Hou, J. G., J. Mat. Sci. Lett. 19 (2000), 963-964. (b) Windes, W. W., Zimmermann, J., and Reimanis, I. E., Surf. and Coat. Tech. 157 (2002) 267-273.

4. (a) Aizenberg, J., Braun, P. V. and Wiltzius, P., Phys. Rev. Lett. 84 (2000), 2997-3000. (b) Choi, W. M. and Park, O. O., Nanotechnology 17 (2006), 325-329.

5. Sun, J., Gao, M., and Feldmann, J., J. Nanosci. Nanotech. 1 (2001), 133-136.

6. Affoune, A. M., Prasad, B. L. V., Sato, H., and Enoki, T., Langmuir 17 (2001), 547-551.

7. (a) Ferrari, B. and Moreno, R., J. Electrochem. Soc. 147 (2000), 2987-2992. (b) Tang, F., Uchikochi, T., Ozawa, K. and Sakka, Y., Mat. Res. Bull. 37 (2002), 653-660. (c) Zanetti, S. M., Varela, J. A., Leite, E. R., and Longo, E., J. European Chem. Soc. 24 (2004) 2445-2451.

1D defect structures in 2D MoO_3 nanostructures on Au(111)

M.M. Biener, J. Biener (LLNL)
X. Deng, S.Y. Quek, D.H. Kang, R. Schalek, E. Kaxiras, C.M. Friend (Harvard University)

Molybdenum oxide is an important commercial catalyst which is widely used in the petroleum and chemical industry. In general, the catalytic properties of metal oxides depend sensitively on the presence and nature of defects. In the case of molybdenum oxides, a high surface oxidation state is expected to be a crucial factor for the partial oxidation of hydrocarbons. On the other hand, the presence of oxygen vacancies plays an important role in enhancing selectivity and reactivity by providing reactive sites. Thus the ability to control quantity and type of defects in the oxides is important, both for fundamental studies and for commercial applications.

In recent years, novel metal oxide nanocrystals have been grown on metal surfaces. This development adds another dimension of interest because these nanocrystals often exhibit structures and electronic properties that are distinct from the bulk phase, and which arise from interface and nanoscale effects. In our own work, we developed a technique which allows us to grow single-layer Mo oxide nanostructures on Au(111) via oxidation of Mo nanoclusters. This single-layer MoO_3 phase is related, but distinctly different to the bulk phase of MoO_3. For example, novel electronic properties arise from the epitaxial misfit strain.

Here, we show that it is possible to control the number of defects in these single-layer MoO_3 nanostructures grown on Au(111) by a simple thermal reduction treatment. The nature of the defect was identified by X-ray photoelectron spectroscopy which reveals the formation of Mo^{5+} species and oxygen vacancies during annealing at 650 K. The amount of Mo^{5+} increases with annealing time, until a stable composition containing 50% Mo^{6+} and 50% Mo^{5+} is reached. The formation of lower oxidation states such as Mo^{4+} was not observed. Scanning tunneling microscopy (STM) reveals the formation of extended one-dimensional shear defects rather than isolated point defects (Figure 1). A possible structural model of a reduced single-layer MoO_3 island is shown in Figure 2. The model assumes the formation of shear planes by a local transformation of corner connected MoO_3 units to edge connected MoO_3 units, and is capable of reproducing the main features observed in the high resolution STM image shown in Figure 1d. Specifically, it predicts the observed shift of the MoO_3 lattice by half a lattice constant between regions

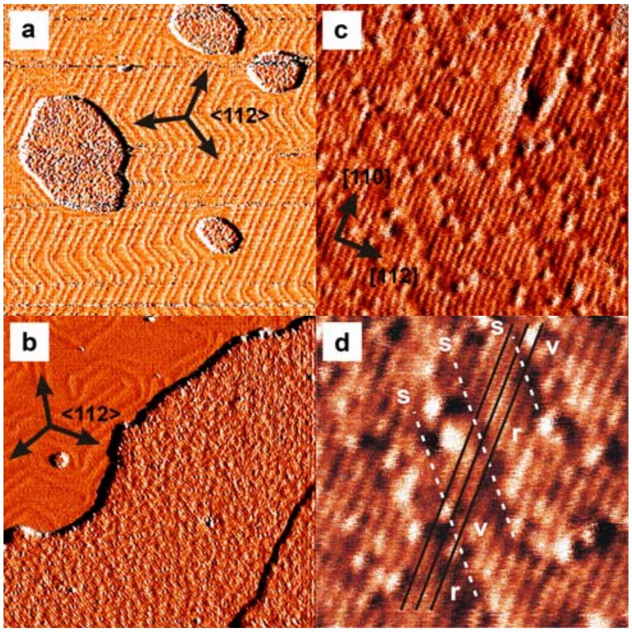

Fig. 1: *STM images collected from MoO_3-covered Au(111) surfaces before (a) and after annealing at > 650K (b-d): (a) Stoichiometric MoO_3 islands on Au(111) prepared (125 nm x 125 nm). (b) Reduced Mo oxide island formed after annealing (85 nm x 85 nm). (c) Higher magnification STM image of the reduced Mo oxide island shown in (b). Despite the appearance of defects, the surface corrugation on top of the island is less than 0.1 nm demonstrating the 2D character of the structure (17 nm x 17 nm). (d) Extended, one-dimensional defects marked by dashed lines (s) appear on top of the Mo oxide islands and separate regions shifted by half a lattice constant. The full lines serve as a visual guide to demonstrate the lattice shift from a valley (v) to a ridge (r) position on opposite sites of the defect (s) (8 nm x 8 nm).*

separated by a shear defect. The driving force for the formation of these shear defects could be the elimination of oxygen vacancies produced by annealing.

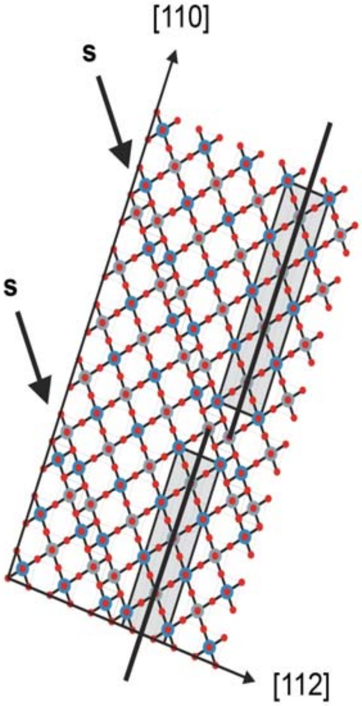

Fig. 2: Structural model of a reduced single-layer MoO_3 island. Note that the presence of 1D shear defects (s) causes a shift of the MoO_3 lattice by half a lattice constant between regions separated by the defect.

The projected density of states of the structural model shown in Figure 2 was calculated by density functional theory (DFT) (figure 3). It can be seen that Mo atoms associated with shear defects have a higher density of states at the Fermi level than those away from the defect or those in the fully-oxidized oxide, suggesting possible enhanced reactivity of Mo along shear lines. The predominant contribution to Fermi level states arises from d states of Mo^{5+} (Figure 3a). The density of states of O bridging atoms in the shear line region is significantly shifted compared to those of corresponding sites far from the defect. This is the result of an increase in coordination number of these O atoms (2 away from the defect and 3 in the defect region), as well as changes in the oxidation state of Mo atoms in the defect region, to which these O bridging atoms are bonded.

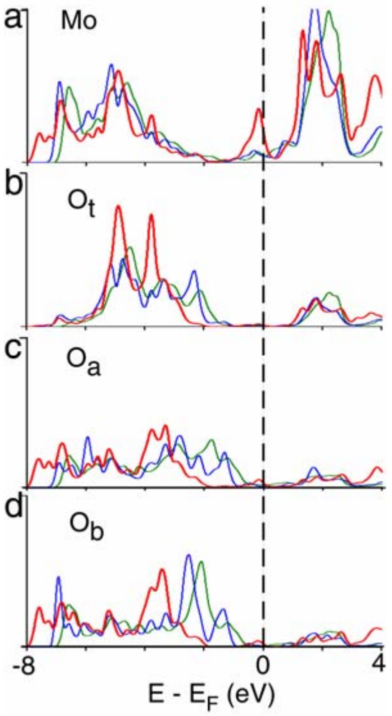

***Fig. 3**: Electronic densities of states projected onto Mo (a), terminal oxygen (b), and the two types of bridging oxygen (c), (d) summed over s, p and d contributions. Red (thickest), blue and green (finest) curves respectively represent atoms at the shear defect, atoms mid-way between the defects in the reduced oxide, and atoms in the fully oxidized oxide, respectively.*

The final composition of 1:1 for the ratio of Mo^{5+} to Mo^{6+} corresponds to the well-defined stoichiometry Mo_4O_{11}. It is interesting that bulk Mo_4O_{11} is the Magneli phase with the highest known density of shear defects. Bulk Mo_4O_{11} has a three-dimensional structure, with layers of Mo_6O_{22} linked by MoO_4 tetrahedra via covalent bonds. It is possible that the final stable Mo_4O_{11} phase observed in our experiments is the two-dimensional analog to the three-dimensional Mo_4O_{11} bulk phase. The ability to control and tailor the oxidation states in these single-layer oxide structures suggests exciting possibilities for future chemical sensor applications.

ZnO nanowire based energy converter

X.Y. Wang, Y.M. Wang, D. Sirbuly, A. Noy, A.V. Hamza

We have fabricated a multifunctional energy nanoconverter, based on stimuli-responsive poly(vinyl chloride-co-vinyl-co-2-hydroxypropyl acrylate) (PVC) and piezoelectric ZnO nanowires. The versatile properties of PVC in response to the changes of the environment, coupled with the piezoelectric and semiconducting nature of ZnO nanowires, enable the hybrid nanodevice to harvest several energy sources, including chemical solvents, thermal energy, vapor energy, and photon energy, into electric-current with the power generation in the range of nano-Walts. The hybrid element thus has potentials to revolutionize energy harvesting in a complex environment where multiple energy sources often co-exist, and might find applications in powering integrated nanoelectronics.

To fabricate such hybrid nanodevice, the ZnO nanowires (NWs) were epitaxially grown on the a-plane (110) sapphire substrate covered with a thin layer of ZnO film, using a chemical vapor transport and condensation (CVTC) process. After growth, NW forest was infiltrated with PVC dioxane solution by drop-casting. The physical and mechanical properties of PVC polymers allow for room-temperature formation of uniform, flexible thin films. Once the PVC film is cured, its top surface was cleaned in oxygen plasma in order to expose NW tips for electrical contacts. The oxygen plasma etching process also helps to remove contamination species such as OH on the NW surface and to form rectifying transport characteristic between Au-ZnO contacts. The top electrode Au/Ti (200nm/50nm) was defined via electron beam evaporation, while the bottom electrode was made of silver paste on ZnO film. Since the PVC polymer is an electrical insulator, in this experimental setup the electric current can only flow through the semiconducting ZnO NWs. Fig. 1 shows the schematic of our experimental setup. An array of vertically-aligned ZnO (n-type) NWs is embedded in stimulus responsive poly(vinyl chloride-co-vinyl-co-2-hydroxypropyl acrylate) (PVC). The PVC film is responsive to the change of environment such as temperature, solvents, vapors, mechanical stress, chemical or biological agents. As a direct outcome of the reactions to the environmental changes, the PVC polymer film deforms microscopically through the stretch or bending of C-Cl, C-H, or C-C bonds, which causes the stretch/bending/compression motion of ZnO NWs and subsequently generate electric current. We are presently investigating the feasibility of such device for energy harvesting applications.

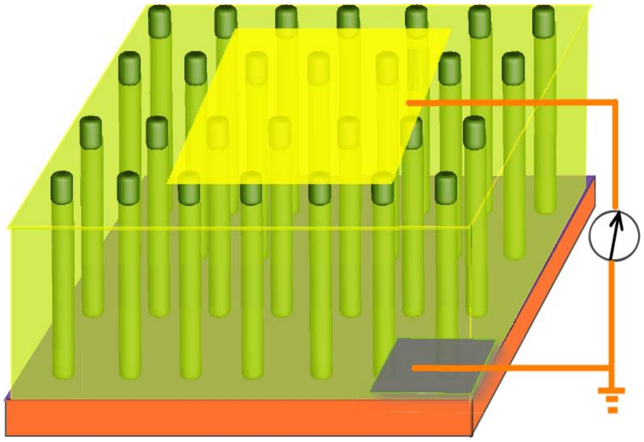

Fig. 1 The schematic of the experimental setup for ZnO nanowire based energy converter.

Segregation and precipitation of Er in Ge

S. O. Kucheyev, T. E. Felter, A. V. Hamza, (LLNL) J. E. Bradby, S. Ruffell, and C. P. Li (Australian National University)

The behavior of Er in Si has been extensively studied for the past decade, stimulated by the drive for integration of photonics and Si technology. In contrast, only a few previous studies have focused on the Ge:Er system. It has previously been demonstrated that, with decreasing size of Ge nanoparticles below a few nanometers, their bandgap rapidly increases. The number of studies of Ge-based nanomaterials, including nanoparticles, nanowires, and nanofoams, is currently growing fast since nanostructured Ge exhibits some advantages over Si. These include stronger quantum confinement effects and better controlled oxidation. In addition, Ge is known to spontaneously develop nanoporosity during ion bombardment under certain irradiation conditions, which could be exploited for the fabrication of novel nanodevices.

Although Er-doped Ge nanostructures have been a subject of previous reports, we are not aware of any studies of the basic properties of Er in Ge, such as diffusivity, solubility, and segregation. Since this information is crucial for the development of Ge:Er-based devices, we have studied the behavior of Er-implanted Ge during annealing with thermal budgets needed for the recovery of crystallinity in a disordered Ge lattice [1]. Our results show that crystallinity is conveniently recovered at temperatures (~400 C) below the onset of significant redistribution of Er, starting at ~500 C. This is an advantage over the Si:Er system, where recrystallization (without co-doping with light elements such as oxygen) is accompanied by complex, concentration and temperature dependent segregation of Er at the amorphous/crystalline (a/c) interface. However, Er forms precipitates in Ge even at ~400 C (see figure). Our results also show that, for temperatures >500 C, Er atoms in Ge are segregated at the a/c interface. The concentration of Er left in the Ge bulk after solid phase epitaxy decreases with increasing annealing temperature but is independent of the initial bulk Er concentration for the ion doses studied here. These findings on the basic behavior of Er in Ge are important for understanding properties of Er-doped Ge nanomaterials.

Reference

[1] S. O. Kucheyev, J. E. Bradby, S. Ruffell, C. P. Li, T. E. Felter and A. V. Hamza, Applied Physics Letters **90**, 221901 (2007).

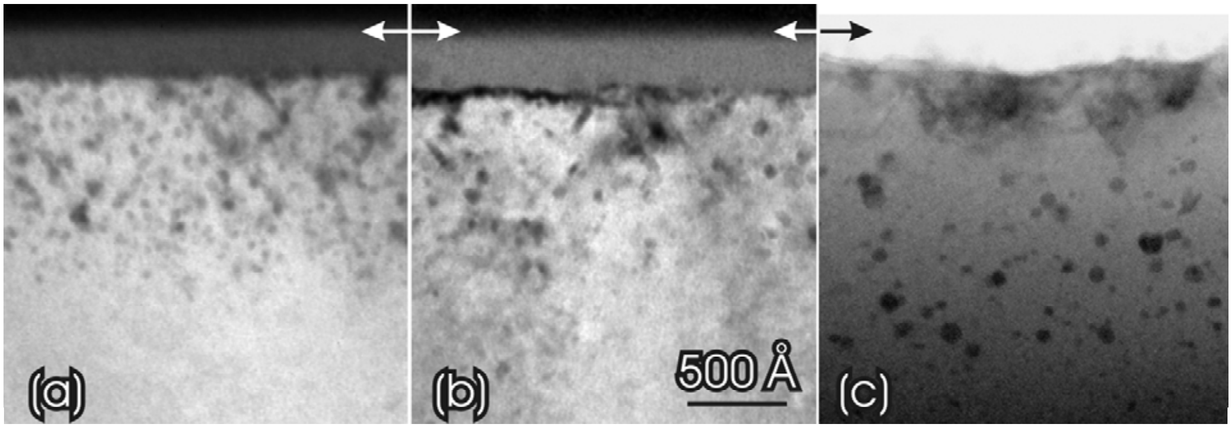

Caption: Bright-field cross-sectional transmission electron microscopy images of Ge bombarded at -196 C with 500 keV Er ions to a dose of 4.4 10^{15} cm^{-2} and annealed at (a) 400, (b) 500, and (c) 800 C. All images are of the same magnification.

Doping of diamond with mid-to-high Z metals

M.M. Biener, J. Biener, S.O. Kucheyev, Y.M. Wang, B. El-Dasher, and Alex V. Hamza (LLNL),
H. Obloh, W. Mueller-Sebert, E. Woerner, A. Kriele, and C. Wild (FHI for Applied Solid-State Physics)

Diamond exhibits a unique combination of properties such as the highest atomic density of any material, extreme strength, high thermal conductivity, and a broad optical transparency. These properties in combination with the ability to grow complex 3D diamond structures via chemical vapor deposition (CVD) makes diamond a very interesting target material for high-energy density (HED) physics experiments. Besides grain structure engineering, doping with mid-to-high Z elements allows one to fine-tune the material properties for this application.

In principle, synthetic diamond grown by CVD can be doped by simply adding any suitable volatile precursor species to the CVD growth process (see Figure 1). However, so far this approach has only been studied for the light elements B, N, P, and S. Here we explore the possibility to extend this approach to mid-to-high Z metals. Based on the following arguments, we selected Mo and W as promising candidates: 1) Volatile precursor species (hexa-carbonyls, MCO_6) are available, and they are compatible with the CVD diamond growth process; 2) both metals form stable metal-carbon bonds which helps to stabilize adsorbed precursor species during the high temperatures typical for the diamond CVD process (700-1000°C); and 3) neither Mo or W are known to catalyze the graphitization of diamond.

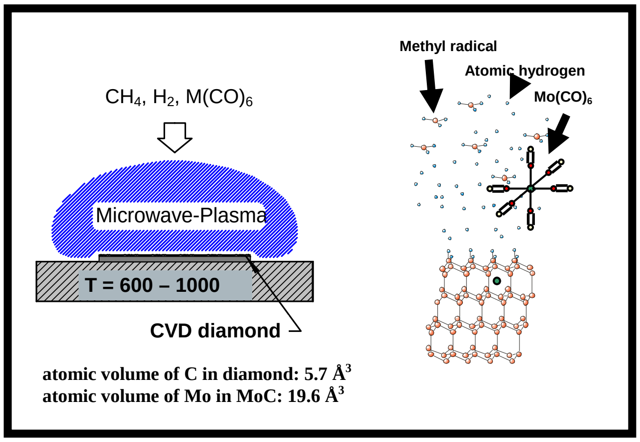

Fig. 1: *Illustration of microwave-assisted chemical vapour deposition of diamond and doping by addition of volatile metal precursors. The growth of CVD diamond is kinetically controlled which should allow one to overcome the thermodynamically unfavourable incorporation of larger metal atoms.*

We systematically studied the influence of various deposition parameters including temperature, precursor partial pressure, and grain structure on the dopant concentration. The spatial distribution of the dopant atoms was determined by secondary ion mass spectroscopy (SIMS) calibrated against Rutherford backscatter spectroscopy (RBS). Our results show that the most important parameter is the deposition temperature, and that the doping level decreases with increasing deposition temperature (Figure 2). On the other hand, the doping level is rather insensitive to the specific grain structure of the deposited material (ranging from nanocrystalline to single crystalline) and the precursor exposure (controlled by the precursor temperature). These observations suggest that the doping level is predominantly controlled by the precursor life

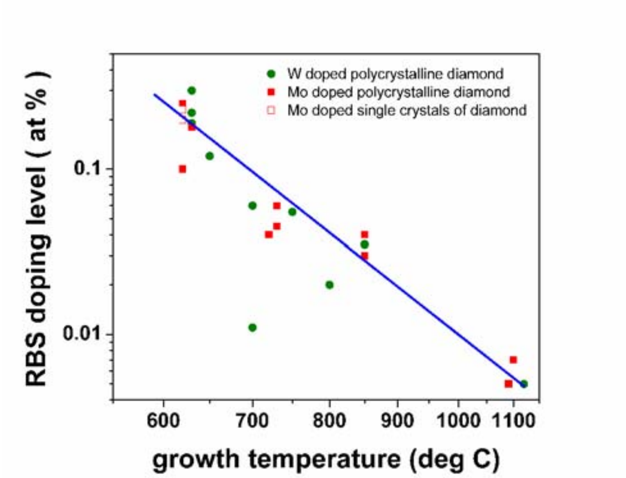

Fig. 2: *Correlation between metal doping level and deposition temperature.*

time under growth conditions. This conclusion is further corroborated by the observation that the doping level depends on the position on the coated diamond wafer. Generally, the highest doping level is found near the edge of the diamond wafer where the precursor is admitted. On the other hand, grain boundary incorporation does not seem to play an important role as almost identical doping levels were observed on polycrystalline and single crystalline diamond films grown at the same temperature (Figure 2). The absence of grain boundary enrichment was also observed by cross-sectional transmission electron microscopy.

Single crystalline Mo-doped diamond samples were grown using single crystal natural diamond substrates with (111), (110), and (100) orientations. The single crystalline character of the deposited material was confirmed by electron backscatter diffraction (EBSD) and Rutherford backscattering (RBS) / channeling experiments. The latter also allowed us to probe the lattice site location of Mo (Figure 3). The observed angular dependence reveals that Mo does not reside on simple substitutional or tetrahedral interstitial sites in the cubic diamond lattice. Most likely, Mo displaces more than one carbon atom in the lattice, whereby assuming a distorted octahedral configuration.

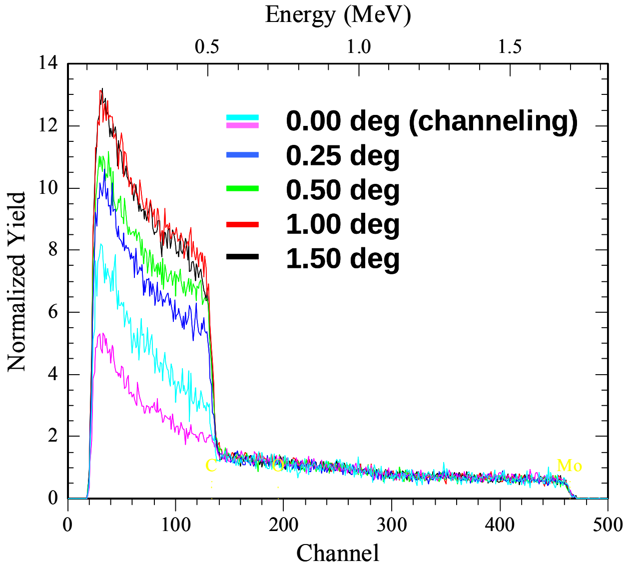

Fig. 3: *Rutherford backscatter/channeling data collected from a ~5-micron-thick Mo-doped diamond film grown on a diamond(100) single crystal substrate.*

One specific application of high Z doping in the context of high resolution x-ray backlighting experiments is to create a contrast which allows one to follow the dynamics of material transport in HED experiments. Figure 4 shows a radiograph obtained from an undoped/doped diamond layer structure (Mo doping level 0.25 at. %) which demonstrates that the doping levels achieved in the present study are sufficient to provide good contrast.

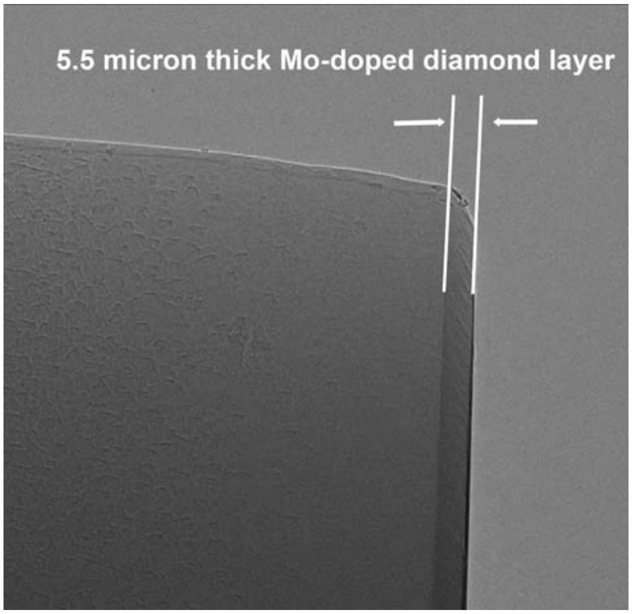

Fig. 4: *Radiograph through a wedge-shaped diamond sample. The 5.5 micron thick Mo-doped diamond film (doping level 0.25 at. %) was deposited at 630 °C on a polished polycrystalline diamond substrate. Note the uniformity of the contrast achieved by Mo doping, and the sharp interface between doped and undoped material. The radiograph was provided by courtesy of N. Teslich, LLNL*

Diamond-metal sandwich structures

M.M. Biener, J. Biener, S.O. Kucheyev, Y.M. Wang, B. and Alex V. Hamza (LLNL),
E. Woerner and C. Wild (FHI for Applied Solid-State Physics)

The material behavior of diamond under the extreme temperature, pressure and strain rate conditions as they appear in shockwaves has recently attracted much interest. VISAR (Velocity Interferometer System for Any Reflector) is the most important experimental technique to measure these properties. Here we demonstrate that it is possible to fabricate gap-free diamond-metal-diamond sandwich structure targets for thermal conductivity measurements where the metal layer provides the necessary reflecting interface. This specific application requires that the metal layer is very thin (in the order of 100 nm) which eliminates the option to prepare such a target structure by soldering of two prefabricated diamond films together (a gap-free solder connection would require a one-micron-thick solder layer).

However, a 100-nm thick metal interface can be realized by growing diamond via chemical vapor deposition (CVD) directly on a metallized diamond surface. Proper choice of the metal coating is crucial, as only a few metals will survive the high temperatures and the corrosive environment typical for diamond CVD. Furthermore, the metal layer must provide good adhesion and nucleation for diamond CVD, and should not catalyze graphitization of diamond. Using the requirements outlined above as guideline, we selected Mo (carbide forming metal) and Pt (non-carbide forming metal) as promising candidates.

First, we studied the thermal stability of 100-nm thick Mo and Pt layers on diamond under high-vacuum conditions in the temperature range from 700-1000 °C by a combination of Rutherford backscatter spectroscopy (RBS) and cross-sectional electron microscopy (SEM and TEM). We observe that both metal films are stable at 700 °C whereas massive diffusion and interface deterioration occurred during annealing at 1000 °C (see Figure 1).

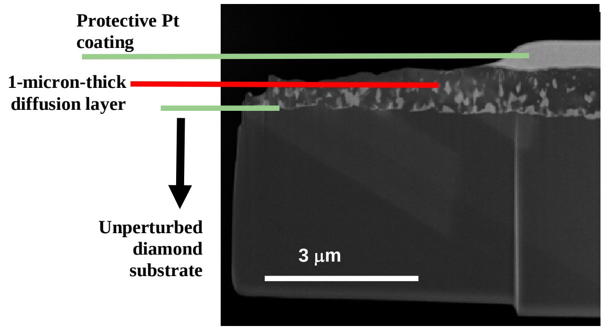

Fig. 1: Cross-sectional SEM image of a FIB lift-out Mo-diamond sample annealed for 8h at 1000 °C. The original 100-nm-thick Mo layer reacted with the diamond substrate, and formed a 1-micron-thick diffusion layer. The heterogeneous structure of this layer indicates carbide formation. The inward diffusion of Mo was also verified by RBS.

Using these results as input, we deposited several micron thick diamond films on Pt-coated optical quality diamond substrates selecting lower-than-usual process temperatures by reducing the microwave plasma power. The adhesion of the Pt layer on diamond was improved by first coating the diamond substrate with a very thin (few nm) Ti adhesion layer. Finally, the sandwich structure is polished to the desired thickness and optical-quality surface finish (see Figure 2).

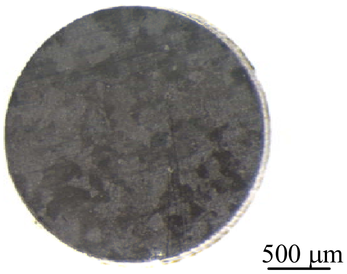

Fig. 2: Optical image of a 2 mm diameter diamond (400 µm)/Ti-Pt (100 nm)/diamond (10 µm) sandwich structure. Note that the grain structure of the buried metal layer is visible through the transparent diamond film.

Homoepitaxial diamond growth on polycrystalline diamond substrates

M.M. Biener, J. Biener, B.S. El-Dasher and Alex V. Hamza (LLNL),
M. Wolfer, E. Woerner and C. Wild (FHI for Applied Solid-State Physics)

The low-pressure growth of diamond via chemical vapor deposition (CVD) has been the subject of intense research. Yet, a unifying atomic scale growth model explaining the observed growth kinetics on different diamond surface orientations has not emerged, and even the simple case of homoepitaxial diamond growth on low index surfaces is still subject to discussion. It is generally observed that the growth rate is a function of the substrate orientation. For example, the fact that CVD diamond typically develops (111) or (100) facets indicates that (110)-oriented surfaces grow considerably faster. Furthermore, it has been demonstrated that the relative growth rates of (111) versus (100) facets can be controlled by the gas phase chemistry. Also step edges have been suggested to play an important role in the CVD growth of diamond, but so far most studies focused on low index surfaces with low step-edge densities.

Here, we report on a study of homoepitaxial diamond growth on polycrystalline, polished CVD diamond substrates. Specifically, we use a combination of electron backscatter diffraction (EBSD) and white- light interferometry which allows us to study the effect of grain orientation and surface morphology on the growth rate. The use of polycrystalline substrates has the advantage that each experiment contains the complete information about the full orientation-growth rate correlation. All samples were characterized before and after deposition of a few hundred nm of CVD diamond (Figure 1). The effect of grain orientation on the growth rate was analyzed by generating orientation-height data sets by combining EBSD and white light data. This task requires the correction of the EBSD grain maps for unavoidable lateral distortions. This is accomplished by automated calculation of the necessary lateral corrections by using unique surface features as landmarks. Finally the orientation height correlation is obtained by averaging the height of all points with the same orientation and plotting the result in a stereographic triangle (Fig. 2).

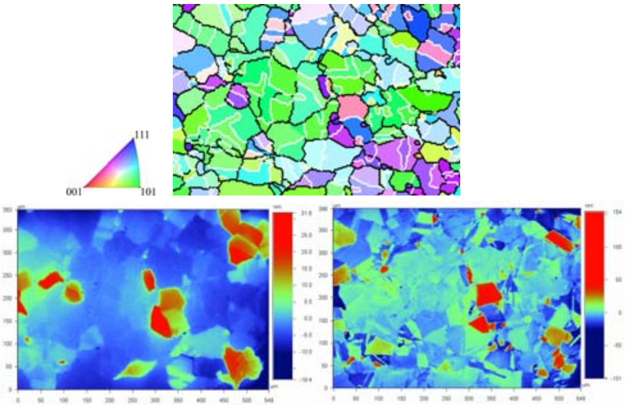

Fig. 1: Top: EBSD grain map (~500 μm x 400 μm) collected from a polished surface of a polycrystalline diamond sample. Bottom: Corresponding white-light images before (left) and after (right) deposition of a few hundred nanometer of diamond. Note the pronounced change in the surface morphology revealing a strong growth rate–orientation correlation.

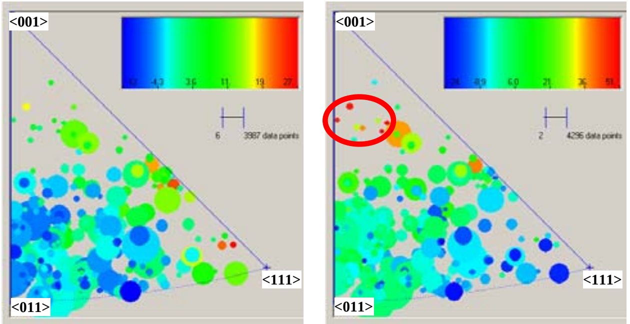

Fig. 2: Height-grain orientation correlation before (left) and after (right) deposition of a few hundred nm of CVD diamond plotted in the standard stereographic triangle. The position of the circles corresponds to their orientation, the color to their height (blue for the lowest and red for the highest grain) and the radius to the amount of data points which were included in the averaging procedure. Note the pronounced relative height change upon diamond deposition.

The preliminary data shown in Fig. 1 and 2 suggest that the (111)-planes grow slower than the (110) or (001) orientated planes. Specifically planes with orientations near the connection line of <001> and <011> seem to be the fastest growing grains (see red circle). Future experiments will address the effect of the growth conditions on this behavior, in particular by systematically varying the relative growth rates on {100} and {111} facets. Increasing the step edge density by a slight misorientation from a low index direction does not seem to have a major impact on the growth rate. However, the concentration of the fastest growing orientation in a relatively small area of the stereographic triangle (see red circle in Fig. 2) points towards the importance of specific sites linked to the presence of step edges.

State-of-the-art process techniques for crystalline carbon NIF targets: seeding and etching

Juergen Biener, Monika M. Biener, and Alex V. Hamza (LLNL),
Christoph Wild , Armin Kriele, and Eckhard Woerner (Fraunhofer Insitute for Applied Solid-State Physics)

Developing a toolbox of state-of-the-art processing techniques for diamond laser targets is necessary to meet the stringent specifications required for inertial confinement fusion (ICF) experiments. In recent years we have perfected polishing and hole drilling techniques which now allow us to achieve a better than required surface finish, and to drill sub-10-micron holes through a 80 micron thick crystalline carbon ablator. Here, we report on our recent progress in improving the surface finish of the *inner* surface and in making the mandrel-removal process through micron-sized holes predictable.

The inner surface finish of NIF ablator capsules is of particular importance for target performance as imperfections give rise to instabilities at the fuel-ablator interface. Due to the templating nature of the capsule fabrication process – CVD diamond is grown on a spherical Si mandrel – defects on the Si mandrel surface will be directly replicated in the diamond film. Avoiding the formation of such template-induced surface defects is crucial as it is impossible to improve the surface finish at a later stage of the capsule fabrication.

Unfortunately, nucleation of diamond on non-diamond substrates (including Si) is difficult and therefore requires a substrate surface pretreatment to achieve the high nucleaction densities ($\geq 10^{14}$ m^{-2}) necessary for the formation of a fully dense, non-porous substrate-diamond interface. Various seeding techniques have been described in the literature, including scratching, biasing, and surface engineering. Scratching is the easiest technique which can be applied to spheres and it does not require modifications to the CVD reactor such as incorporation of a bias electrode. A typical SEM image of the nucleation regime of CVD diamond growth is shown in Fig. 1.

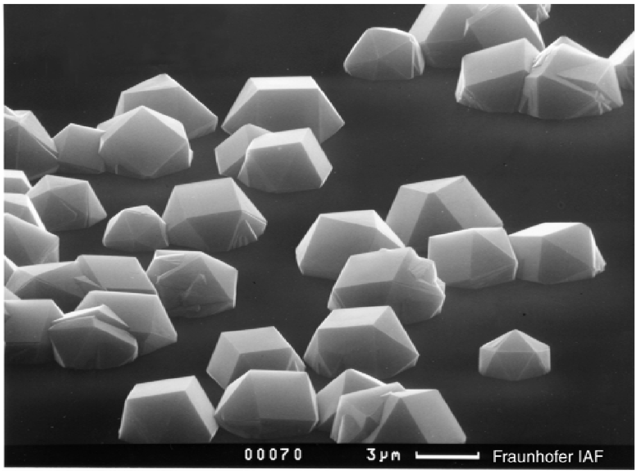

Fig. 1: SEM micrograph showing the nucleation regime of CVD diamond growth.

The key to obtain a high quality finish of the shell inner surface is to optimize the nucleation density while minimizing the number of surface defects created by the surface preparation treatment. On flat substrates good results are obtained by manual application of diamond slurry. The technique is less suited for the spherical mandrels used in the fabrication of NIF diamond ablator shells, where we apply a modified mechanical treatment (scratching) consisting of ultrasonic agitation in a methanol suspension of diamond powder. The quality of the inner surface finish critically depends on the specific parameter set used in this process. For example, coarse-grained diamond powder tends to create larger defects than nanocrystalline

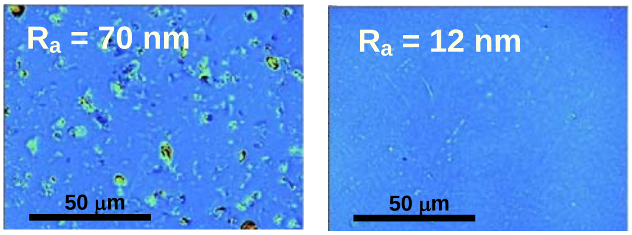

***Fig. 2:** Scanning white-light interferometer images of diamond shell inner surfaces. The surface roughness decreases by a factor of 5 by using more gentle seeding conditions.*

diamond powders. The example show in Fig. 2 underlines the importance of finding a gentle, yet efficient pretreatment procedure. Future work includes modification of our CVD reactor to allow for bias enhanced nucleation (BEN) which is known to result in minimal substrate damage and very high nucleation densities. Here, a negative bias in the order of a few hundred volts is applied to the substrate during the nucleation regime which causes the formation of a SiC layer.

Another focus point of our activities was to obtain a better understanding of the mandrel etch process. To remove the solid Si mandrel used in the diamond CVD process through a small hole fabricated by laser or focused ion beam (FIB) microfabrication techniques, we developed a ultrasonically assisted HF/HNO_3 wet etch process. Although early experiments on shells with relatively large holes were promising (removing the mandrel though a > 20 micron diameter hole typically requires a few days), it was not clear which diameter dependence the etch process would follow. Assuming laminar flow through a capillary, one would expect that the mass transport scales with d^4, where d is the hole diameter. Thus decreasing the hole diameter by a factor of 4 from 20 micron to 5 micron would cause a 256 fold decrease in the etch rate. With other words, mandrel removal through a 5 micron hole could take as long a one year. Therefore, removing the solid Si mandrel through a 5 micron diameter and 80 micron long hole was considered to be a high risk milestone.

To better assess the risks, we designed a experiment which allowed us to measure the etch rate as a function of hole diameter. In short, we exploit the optical transparency of diamond to assess the etch rate through micron-sized holes using a microscope. As samples we used small rectangular pieces of Si coated with optical-quality diamond films of various thicknesses. The diamond surface was polished, and well-defined micron-sized holes were drilled through the diamond capping layer using FIB microfabrication. The Si etch rate through these holes was then assessed by assuming a spherical shape of the etched volume (Fig. 3). The resulting diameter dependence of the etch rate is shown in Fig. 4.

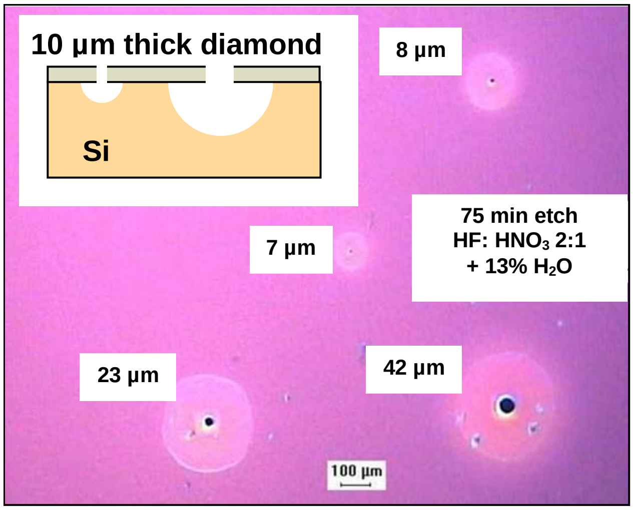

Fig.3: Optical image of a Si wafer coated with a 10-micron-thick diamond film with FIB drilled holes through the diamond film (diameter ranging from 7 micron to 42 micron). The image was taken after 75 min of etching using an ultrasonically assisted HF/HNO_3 wet etch process. The diameter of the halo surrounding each hole allows one to estimate the amount of removed material.

The experimentally observed diameter dependence of the Si etch rate is much weaker than expected, $d^{1.25}$ versus d^4, pointing towards the importance of ultrasonically enhanced mass transport. Based on the measured etch rates shown in Fig. 4. the removal of a 2 mm diameter mandrel through a 5 micron hole will take ~1 month, a value which has recently been verified.

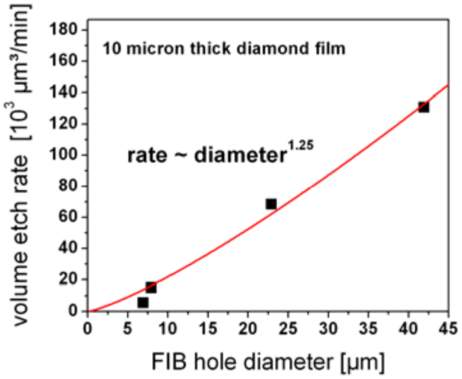

Fig. 3: *Etch rate of Si through FIB fabricated holes using an ultrasonically assisted HF/HNO_3 wet etch process. Note the weak diameter dependence.*

New gold and silver-gold catalysts in the shape of sponges and sieves

J. Biener, M.M. Biener, and A.V. Hamza, LLNL
B. Jurgens, C. Schulz, T. Nowitzki, V. Zielasek, and M. Baeumer, University of Bremen
C. Kuebel, Fraunhofer Institute for Manufacturing Technology and Applied Materials Science (IFAM)

Since the first report on CO oxidation over Au nanoparticles in the 1980s, the unexpected catalytic activity of gold, which is inert as a bulk material, has been the target of intense research. What makes gold unique as a catalyst material is its ability to efficiently catalyze oxidation reactions even at low temperatures where other metals are no longer active. However, the active states of gold responsible for oxidation are still the subject of intense debate, and explanations range from nanoscale effects to particle-support interactions to cationic Au species. Despite this controversy, there is general agreement that low-coordinated Au surface sites are a necessary prerequisite. At such sites, oxygen is more easily dissociated and CO binds more strongly.[1]

In our work, we have demonstrated that *unsupported* nanoporous gold, generated by dealloying a AgAu alloy, exhibits significant catalytic activity with respect to CO oxidation at temperatures as low as 0°C.[2] Since Ag is not be completely removed from the material, Ag residues at the surface of nanoporous Au may be involved in the catalytic cycle. To address this question, we developed a Y-zeolite-based model system where the influence of the Ag could be investigated in a systematic manner by loading zeolites with Au or bimetallic Au/Ag nanoparticles.[3] We observe that Ag significantly increases the activity of the zeolite system towards CO oxidation in the temperature range from -20 to 50°C, probably due to activation/dissociation of molecular oxygen by silver (see Figure 1).

The loading of the zeolite with gold and bimetallic gold/silver nanoparticles was verified by 3D Scanning Transmission Electron Microscopy tomography. The images reveal that it is possible to incorporated gold and bimetallic gold/silver nanoparticles in the zeolite lattice. The highest catalytic activity was observed at a Ag/Au weight ratio around 0.3:1 (see Figure 1).

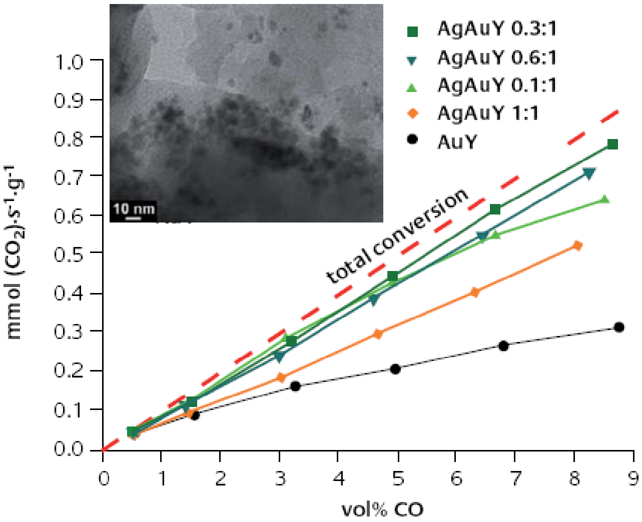

Fig. 1: CO to CO_2 conversion at room temperature as a function of the Ag/Au weight ratio for zeolite catalysts. The activity of bimetallic catalysts is higher than that of monometallic AuY catalysts for all Ag amounts studied. Insert: TEM micrograph of freshly prepared Y-zeolite doped with bimetallic Ag/Au nanoparticles (weight ratio: 0.6 : 1).

These observations suggest that the high catalytic activity of nanoporous gold, which is an unsupported gold catalyst, is caused by residual Ag (4 – 20%) on the surface of the ligaments. It is not yet clear whether Ag intermixes with Au or forms islands of Ag or Ag oxide. The distribution of the silver atoms could play an important role in the catalytic mechanism. Subsurface oxygen may form in the case of larger Ag patches and is known to influence the reactivity of surface oxygen.

1. Yim, W.L., et al., *Universal phenomena of CO adsorption on gold surfaces with low-coordinated sites.* J. Phys. Chem. C, 2007. **111**(1): p. 445-451.
2. Zielasek, V., et al., *Gold catalysts: Nanoporous gold foams.* Angew. Chem.-Intl. Ed., 2006. **45**(48): p. 8241-8244.
3. Jurgens, B., et al., *New gold and silver-gold catalysts in the shape of sponges and sieves.* Gold Bulletin, 2007. **40**(2): p. 142-149.

Controlling the Structure of a Quantum Solid: Hydrogen

G. Gilmer, Y. Han, B. Sadigh, B. Kozioziemski, A. Chernov, and A. V. Hamza

Molecular hydrogen has unique properties that are useful for controlling the morphology of its crystals during growth. The hydrogen isotopes, H2, D2 and T2, form crystalline phases with strong quantum properties that affect molecular mobility, surface properties, and bulk lattice constants. Unlike helium, the relatively low triple point pressures allow convenient crystal growth from either the vapor or liquid phase. On the other hand, the weak van der Waals bonding between molecules leads to low cohesive energies of crystalline hydrogen, ~0.01eV per molecule, and large vapor densities which can readily transport large molecular fluxes during vapor deposition. Methods for growing hydrogen crystals with precisely determined morphologies are needed for a number of applications, including inertial confinement fusion. In this case, the loading of a beryllium target shell with crystalline DT is a challenging process, because of the strict specifications on DT surface roughness that are required for reaching high densities during the laser induced implosion. The goal of this project is to increase the understanding of hydrogen crystallization by developing molecular dynamics (MD) simulations and experiments than yield information on the fundamental processes that are involved. The MD simulations are providing data at the molecular level, as needed for a complete description of the various types of nucleation, step dynamics, and defect generation that are present during crystallization. Experiments on our newly designed cold stage are being used to examine the dramatic effects of growth conditions on the morphologies.

Recently there has been much activity on the use of templates to provide preferred sites for nucleation, to fix the orientation of the crystals, and, in some cases, to choose between competing crystalline phases. Hydrogen is strongly susceptible to the influence of templates, since the cohesive energy of the first one or two molecular layers on the templates is stronger than that of the bulk solid. Hydrogen molecules bond more strongly to most templates, because of the higher density of electrons in most materials, relative to hydrogen. We are examining the effect of templates on the growth of molecular hydrogen crystals at the molecular level using MD simulations.

We have implemented an MD algorithm that accounts for quantum zero point motion. The classical potential energy for an atomic configuration is given by:

$$U(\bar{r}_1,...,\bar{r}_N) = \frac{1}{2}\sum_{i\neq j} V\left(\left|\bar{r}_i - \bar{r}_j\right|\right)$$

where U is the total potential energy, r_i the molecular coordinates, and V is the interaction energy of an H2 with a neighbor. Zero-point vibrations are approximately included by using a Gaussian probability distribution to mimic the quantum uncertainty:

$$U(\bar{r}_1,...,\bar{r}_N) = \sum_{i\neq j}\iint G(\bar{r}-\bar{r}_i)\cdot V(\bar{r}_i-\bar{r}_j)\cdot G(\bar{r}'-\bar{r}_j)\cdot d\bar{r}d\bar{r}',$$

where G is a Gaussian function with a single fitting parameter σ. The fitting parameter is determined by path integral quantum Monte Carlo calculations.

Simulations of solidification of D2 on planar templates are shown in Fig. 1. The amorphous template induces amorphous D2, whereas the crystalline templates tend to induce crystalline order in the solidified D2. However, the diamond substrate does not order the D2 significantly. The close spacing of the diamond atoms relative to the spacing between D2 molecules is quite large; the lattice mismatch between the gold template and D2 is -9%, and for diamond it is -30%. The potential energy variations for a D2 molecule moving across the template, and hence the influence of the template on film structure, is quite small.

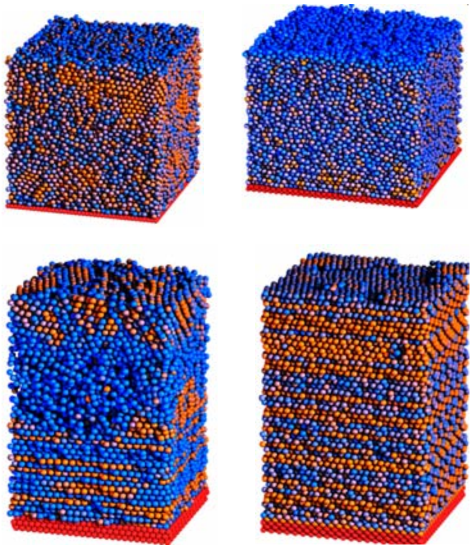

Figure1. Molecular D_2 melt is placed in contact with different templates, and then solidified at a temperature 8K below the triple point. The 40% undercooling produces rapid solidification, and structures that vary with the substrate. An amorphous template, (a), induces an amorphous D_2 structure with some evidence of ordered regions; (b) a diamond template oriented (111) also results in amorphous D_2; (c) a gold template oriented (111) induced a region close to the template with close-packed layers containing small stacking faults; and (d) gold oriented (100) resulted in the greatest degree of order, but with frequent stacking faults between the layers.

We have built a cryogenic chamber for experiments on templated growth. The chamber can accommodate four different templates, and Fig. 2 shows some results on diamond substrates that have been processed in different ways. These results show that the roughening induced by oxidation, Fig. 2(a), provides the best wetting of the template and superior orientation control compared with the other diamond surfaces; comparisons with simulations indicate that the presence of a large numbers of steps is effective in the case of poor lattice matching. Currently work on single crystal Au surfaces is being pursued in experiments, where the simulations predict that superior control over the crystal orientation can be obtained. Other aspects of hydrogen isotope crystallization have been investigated including (i) modeling helium solid solutions and the nucleation of helium bubbles, (ii) the mechanical properties of films and columns of solid hydrogen under stress, and (iii) crystallization effects on the composition of D2 - T2 alloys.

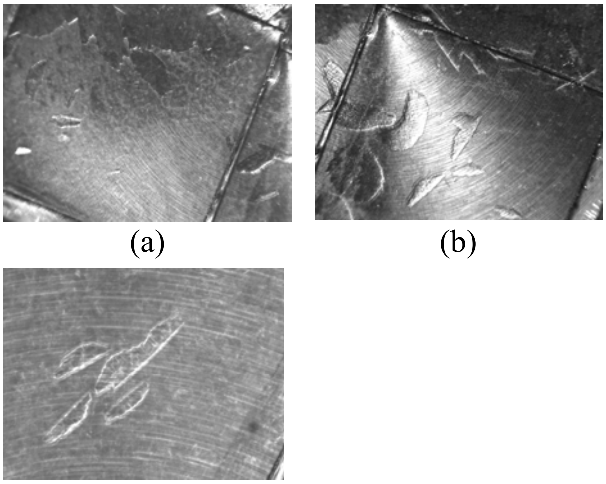

(a) (b)

(c)

Figure 2. Shown are the morphologies of molecular D_2 crystals deposited onto three different templates. Polycrystalline diamond was processed in different ways. In (a), the diamond was oxidized, producing a rough surface; in (b) the diamond template was etched by an argon plasma; and in (c) the diamond was covered with an amorphous graphitic layer.

In conclusion, we have developed efficient computer simulation models and constructed a cryogenic stage for experiments to study the crystallization of molecular hydrogen on flat templates. Our simulations and experiments on the effects of different templates indicate that lattice matching gives the best orientation control of the hydrogen crystals, but that processing a template so as to increase roughening may improve the orientation control for systems with large lattice mismatch.

Acquisition of a dual reactor type atomic layer deposition system designed to allow both dynamic flow and static dosing of precursors

S. Ghosal, J. Biener, S. O. Kucheyev, A. V. Hamza

Nanoporous materials have significant technological potential given the combination of unique physical and chemical properties, and as such, they represent an area of active research interest. Atomic layer deposition offers an attractive method for the fabrication of nanoporous metals based on a template approach as well as the controlled doping of nanoporous materials. The ALD process utilizes a suitable pair of sequential, self-limiting surface reactions and therefore offers excellent atomic level control of the deposited film thickness. Control of the structural features of the nanoporous materials is afforded by the nanocellular templates which have extremely high aspect ratios ~10^5. Uniform coating of such high aspect ratio materials by ALD necessitates careful selection of the deposition conditions.

Traditionally ALD has been used for coating low aspect ratio flat, nonporous materials relevant to the semiconductor industry. Therefore, commercially available ALD reactors are not optimized for coating high aspect ratio substrates with variable dimensions. Infusion of metal precursors into a nanoporous material is limited by the high aspect ratio of its pore structure. Therefore, uniform coating of these materials often requires longer exposure times compared to nonporous samples. In conventional ALD reactors with continuous precursor flow during the deposition process, longer exposure times would result in increasing waste of precursors. However, a static dosing option whereby the reactor is backfilled with precursor at a given pressure would allow for longer exposure times while limiting precursor waste. Furthermore, detailed understanding of the ALD growth process on these non-traditional substrates necessitates the use of high vacuum based surface sensitive analytical tools, such as x-ray photoelectron spectroscopy. Therefore, for successful ALD on nanoporous materials a modified reactor design is necessary to accommodate the dosing and analytical requirements mentioned above.

The Nanoscale Synthesis and Characterization Laboratory is acquiring a novel dual dosing (static and continuous flow) mode ALD reactor (Fig 1) designed by Kurt J. Lesker for deposition on flat as well as high aspect ratio substrates. Some of the challenges facing the static dosing method are – 1) maintenance of precursor pressure in the reactor during dosing, 2) protection of the analytical ports and reactor walls from precursor contamination. Both of theses concerns have been addressed in the new reactor design through the installation of an automated reactor pressure maintenance system as well as the addition of gate valves and heated chamber walls for minimizing contamination during dosing. The stainless reactor is designed to accommodate variable substrate geometry (up to 6” in diameter) with up to 400ºC in substrate heating. Additionally, it comes equipped with two analytical ports for in-situ analysis and is high vacuum compatible. The precursor delivery system can handle up to four precursors, both high and low vapor pressure reactants as well as gases.

The precursors are housed in a vented cabinet and introduced into the reactor through heated lines. The system has automatic process control capability that can be used to run customized deposition processes. Given its versatility the new ALD system will make important contributions to a variety of applications relevant to the laboratory's missions and as such will be a valuable addition to the laboratory's synthetic capabilities.

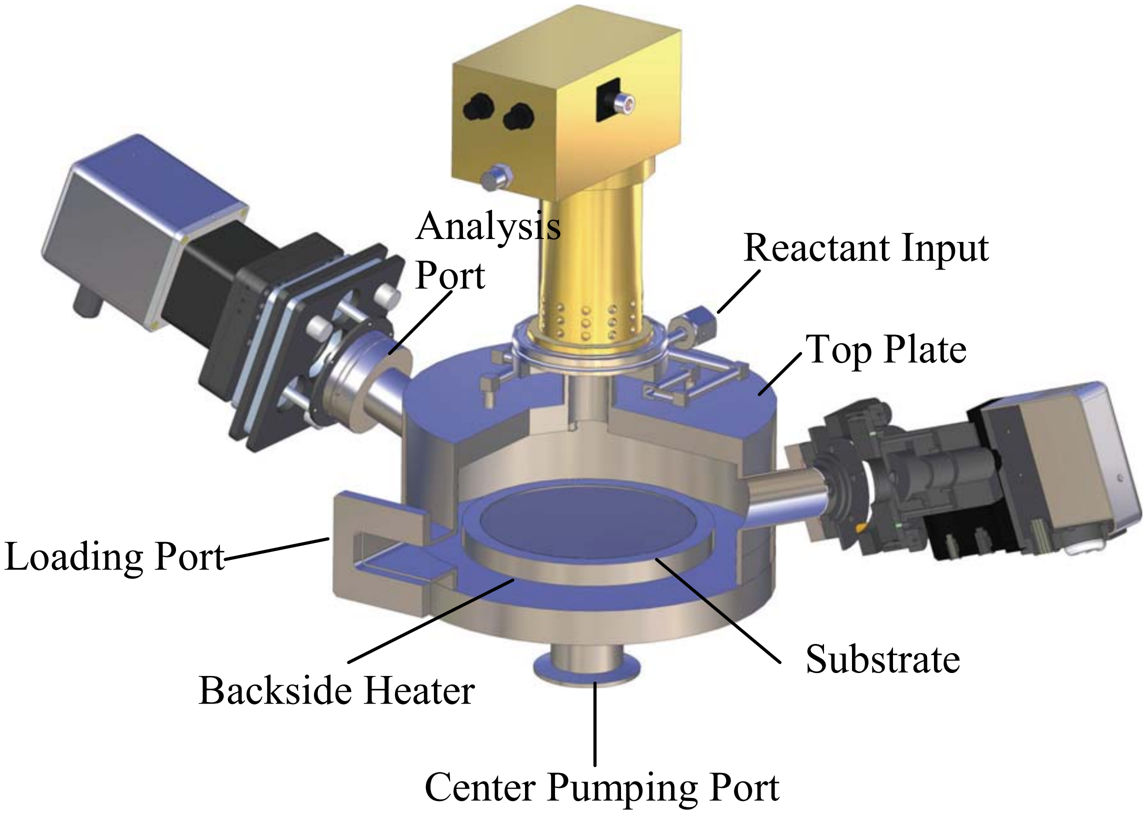

Figure 1. *Dual dosing mode ALD reactor by Kurt J. Lesker.*

Collaborations FY 2007

1. Markku Leskela, University of Helsinki, Atomic Layer Deposition.
2. Stacy Bent, Stanford University, Atomic Layer Deposition.
3. John Rogers, University of Illinois, Urbana-Champaign, Proximity field nanopatterning.
4. Christoph Wild and Eckart Woerner, Fraunhofer Institute for Applied Solid State Physics, Nanograined Diamond Science and Technology.
5. Marcus Baeumer, University of Bremen, Nanoporous gold and nanostructures on gold surfaces.
6. Cynthia Friend, Harvard University, Nanostructures on gold surfaces
7. Heather Wilkens, General Atomics, Advanced hohlraums
8. Cynthia Volkert, Research Center Karlsruhe, Mechanics of nanoporous metals
9. Abbas Nikroo and Hongwei Xu and Mark Conyers, General Atomics, Low stress Be films
10. Roy Gordon, Harvard University, Atomic layer deposition
11. Jorg Weismuller, Research Center Karlsruhe, Nanoporous actuation
12. Ju Li, Ohio State University, Molecular dynamics simulations
13. Eric Chason, Brown University, Stress evolution in film deposition
14. Xian Ying Wang, Shanghai University, Nanodevices
15. John Verboncoeur, University of California, Berkeley, Plasma simulation
16. Andrea Hodge, University of Southern California, Nanomechanics
17. C. Kuebel, Fraunhofer Insitute for Manufacturing Technology and Applied Materials Science
18. M. Toth, W. R. Knowles, FEI Company, Low-vacuum electron microscopy imaging of low-density nanoporous solids.
19. B. L. Thiel, V. Tileli, University at Albany-SUNY, Low-vacuum electron microscopy imaging of low-density nanoporous solids.
20. J. Ilavsky, Argonne National Laboratory, Small-angle x-ray scattering.
21. J. E. Bradby, S. Ruffell, and C. P. Li, The Australian National University, Low-density nanoporous germanium.

NSCL Publications 2007

Amendt, P., Cerjan, C., Hamza, A., Hinkel, D. E., Milovich, J. L., Robey, H. F., “Assessing the prospects for achieving double-shell ignition on the National Ignition Facility using vacuum hohlraums,” PHYSICS OF PLASMAS **14** (5): Art. No. 056312 MAY 2007.

Aufderheide, M. B., III, Brown, W. D., Hamza, A. V., Park, H.-S., Martz, H. E., Remington, B. A., Rogers, J. A., Jeon, S., Nam, Y.-S., “Analysis and modeling of phase contrast radiography of gradient density laser targets,” NUCLEAR INSTRUMENTS & METHODS A- **579** (1): 223-226 AUG 21 2007

Azarov, A. Yu., Kucheyev, S. O., Titov, A. I., Karaseov, P. A., “Effect of the density of collision cascades on ion implantation damage in ZnO,” JOURNAL OF APPLIED PHYSICS **102** (8) Article No. 083547 OCT 15 2007

Biener, M. M., Biener J., Hodge, A. M., and Hamza, A. V., “Dislocation nucleation in bcc Ta single crystals studied by nanoindentation,” PHYSICAL REVIEW B **76**, 165422 (2007)

Biener, M. M., Biener, J., Friend, C. M., “Sulfur-induced mobilization of Au surface atoms on Au(111) studied by real-time STM,” SURFACE SCIENCE **601** (7): 1659-1667 APR 1 2007

Biener, J., Baumann, T. F., Wang, Y. M., Nelson, E. J., Kucheyev, S. O., Hamza, A. V., Kemell, M., Ritala, M., Leskela, M., “Ruthenium/aerogel nanocomposites via atomic layer deposition,” NANOTECHNOLOGY **18** (5): Art. No. 055303 FEB 7 2007

Bono, M., Bennett, D., Castro, C., Satcher, J., Poco, J., Brown, B., Martz, H., Teslich, N., Hibbard, R., Hamza, A., Amendt, P., Robey, H., Milovich, J, Wallace, R., “Fabrication of double shell targets with a glass inner capsule supported by SiO2 aerogel for shots on the Omega laser in 2006,” FUSION SCIENCE AND TECHNOLOGY **51** (4): 611-625 MAY 2007.

Bringa, E. M., Kucheyev, S. O., Loeffler, M. J., Baragiola, R. A., Tielens, A. G. G. M., Dai, Z. R., Graham, G., Bajt, S., Bradley, J. P., Dukes, C. A., Felter, T. E., Torres, D. F., van Breugel, W. “Energetic processing of interstellar silicate grains by cosmic rays,” ASTROPHYSICAL JOURNAL **662** (1) 372-378 Part 1 JUN 10 2007

Hayes, J. R., Nyce, G. W., Kuntz, J. D., Satcher, J. H., Hamza, A. V., “Synthesis of bi-modal nanoporous Cu, CuO and Cu$_2$O monoliths with tailored porosity,” NANOTECHNOLOGY **18** (27): Art. No. 275602 JUL 11 2007.

Hodge, A. M., Biener, J., Hayes, J. R., Bythrow, P. M., Volkert, C. A., Hamza, A. V., “Scaling equation for yield strength of nanoporous open-cell foams,” ACTA MATERIALIA **55** (4): 1343-1349 FEB 2007.

Jeon, S., Nam, Y.-K., Shir, D. J.-L., Rogers, J. A. and Hamza, A., “Three dimensional nanoporous density graded materials formed by optical exposures through conformable phase masks,” APPLIED PHYSICS LETTERS **89**, 253101 (2006).

Juergens, B., Kuebel, C., Schulz, C., Nowitzki, T., Zielasek, V., Biener, J., Biener, M. M., Hamza, A. V., Baeumer, M., “New gold and silver-gold catalysts in the shape of sponges and sieves,” GOLD BULLETIN **40** (2): 142-149 2007

Kucheyev, S. O., Clapsaddle, B. J., Wang, Y. M., van Buuren, T., Hamza, A. V., “Electronic structure of nanoporous ceria from x-ray absorption spectroscopy and atomic multiplet calculations,” PHYSICAL REVIEW B **76**(23) Art No. 235420 DEC 2007

Kucheyev, S. O., Bradby, J. E., Li, C. P., Ruffell, S., van Buuren, T., Felter, T. E., “Effects of carbon on ion-implantation-induced disorder in GaN,” APPLIED PHYSICS LETTERS **91** (26) Article No. 261905 DEC 24 2007

Kucheyev, S. O., Sadigh, B., Baumann, T. F., Wang, Y. M., Felter, T. E., van Buuren, T., Gash, A. E., Satcher, J. H., Jr., Hamza, A. V. “Electronic structure of chromia aerogels from soft x-ray absorption spectroscopy,” JOURNAL OF APPLIED PHYSICS **101** (12): Art. No. 124315 JUN 15 2007

Kucheyev, S. O., Bradby, J. E., Ruffell, S., Li, C. P., Felter, T. E., Hamza, A. V. “Segregation and precipitation of Er in Ge,” APPLIED PHYSICS LETTERS **90** (22): Art. No. 221901 MAY 28 2007

Kucheyev, S. O., Toth, M., Baumann, T. F., Hamza, A. V., Ilavsky, J., Knowles, W. R., Saw, C. K., Thiel, B. L., Tileli, V., van Buuren, T., Wang, Y. M., Willey, T. M., “Structure of low-density nanoporous dielectrics revealed by low-vacuum electron microscopy and small-angle X-ray scattering,” LANGMUIR **23** (2): 353-356 JAN 16 2007

Nyce, G. W, Hayes, J. R., Hamza, A. V., Satcher, J. H., “Synthesis and characterization of hierarchical porous gold materials,” CHEMISTRY OF MATERIALS **19** (3): 344-346 FEB 6 2007.

Smith, R. F., Lorenz, K. T., Ho, D., Remington, B. A., Hamza, A., Rogers, J. A., Pollaine, S., Jeon, S., Nam, Y. K., Kilkenny, J., “Graded-density reservoirs for accessing high stress low temperature material states,” ASTROPHYSICS AND SPACE SCIENCE **307** (1-3): 269-272 JAN 2007.

Titov, A. I., Azarov, A. Yu., Nikulina, L. M., Kucheyev, S. O., “Damage buildup and the molecular effect in Si bombarded with PFn cluster ions,” NUCLEAR INSTRUMENTS & METHODS B **256** (1) 207-210 MAR 2007

Wang, Y. M., Li, J., Hamza, A. V., Barbee, T. W., Jr., “Ductile crystal line-amorphous nanolaminates,” PROCEEDINGS OF THE NATIONAL ACADEMY OF SCIENCES OF THE UNITED STATES OF AMERICA **104** (27): 11155-11160 JUL 3 2007

Wang, Y. M., Hamza, A. V., Barbee, T. W., Jr. “Incipient plasticity in metallic glass modulated nanolaminates**,”** APPLIED PHYSICS LETTERS **91** (6): Art. No. 061924 AUG 6 2007

Wang, Y. M., Jankowski, A. F., Hamza, A. V. “Strength and thermal stability of nanocrystalline gold alloys,” SCRIPTA MATERIALIA **57** (4): 301-304 AUG 2007

Wang, Y. M., Huang, J. Y., Jiao, T., Zhu, Y. T., Hamza, A. V., "Abnormal strain hardening in nanostructured titanium at high strain rates and large strains," JOURNAL OF MATERIALS SCIENCE **42** (5): 1751-1756 MAR 2007.

Yim, W.-L., Nowitzki, T., Necke, M., Schnars, H., Nickut, P., Biener, J., Biener, M. M., Zielasek, V., Al-Shamery, K., Kluner, T., Baumer, M., "Universal phenomena of CO adsorption on gold surfaces with low-coordinated sites," JOURNAL OF PHYSICAL CHEMISTRY C **111** (1): 445-451 JAN 11 2007

Yu, J., Wang, Y.M., Moore, R. L., Lu, J.-Q., Gutmann, R. J., "Low-temperature titanium-based wafer bonding Ti/Si, Ti/SiO2, and Ti/Ti," JOURNAL OF THE ELECTROCHEMICAL SOCIETY **154** (1): H20-H25 2007

Zepeda-Ruiz, L. A., Sadigh, B., Biener, J., Hodge, A. M., Hamza, A. V., "Mechanical response of freestanding Au nanopillars under compression," APPLIED PHYSICS LETTERS **91** (10): Art. No. 101907 SEP 3 2007